JGR Space Physics

RESEARCH ARTICLE
10.1029/2023JA031676

Upper Limit on Outer Radiation Belt Electron Flux Based on Dynamical Equilibrium

D. Mourenas[1,2], A. V. Artemyev[3], X.-J. Zhang[3,4], and V. Angelopoulos[3]

[1]CEA, DAM, DIF, Arpajon, France, [2]Laboratoire Matière en Conditions Extrêmes, Paris-Saclay University, CEA, Bruyères-le-Châtel, France, [3]Department of Earth, Planetary, and Space Sciences, University of California, Los Angeles, CA, USA, [4]Department of Physics, University of Texas at Dallas, Richardson, TX, USA

Key Points:

- Equilibrium upper limits on electron flux are provided in the presence of injections and chorus-driven energy and pitch-angle diffusion
- The steady-state attractor for combined energy and pitch-angle diffusion can determine the upper flux energy spectrum
- Comparisons with maximum electron fluxes measured during strong injection events show a good agreement at 0.1–0.6 MeV

Correspondence to:
D. Mourenas,
didier.mourenas@cea.fr

Citation:
Mourenas, D., Artemyev, A. V., Zhang, X.-J., & Angelopoulos, V. (2023). Upper limit on outer radiation belt electron flux based on dynamical equilibrium. *Journal of Geophysical Research: Space Physics*, *128*, e2023JA031676. https://doi.org/10.1029/2023JA031676

Received 7 MAY 2023
Accepted 6 AUG 2023

Abstract In the Earth's radiation belts, an upper limit on the electron flux is expected to be imposed by the Kennel-Petschek mechanism, through the generation of exponentially more intense whistler-mode waves as the trapped flux increases above this upper limit, leading to fast electron pitch-angle diffusion and precipitation into the atmosphere. Here, we examine a different upper limit, corresponding to a dynamical equilibrium in the presence of energetic electron injections and both pitch-angle and energy diffusion by whistler-mode chorus waves. We first show that during sustained injections, the electron flux energy spectrum tends toward a steady-state attractor resulting from combined chorus wave-driven energy and pitch-angle diffusion. We derive simple analytical expressions for this steady-state energy spectrum in a wide parameter range, in agreement with simulations. Approximate analytical expressions for the corresponding equilibrium upper limit on the electron flux are provided as a function of the strength of energetic electron injections from the plasma sheet. The analytical steady-state energy spectrum is also compared with maximum electron fluxes measured in the outer radiation belt during several geomagnetic storms with strong injections, showing a good agreement at 100–600 keV.

1. Introduction

Outside the plasmasphere, the dynamics of energetic electron fluxes in the Earth's outer radiation belt is determined by injections from the plasma sheet, inward radial diffusion by ultralow frequency waves, and resonant interactions between electrons and whistler-mode chorus or electromagnetic ion cyclotron (EMIC) waves (e.g., see Camporeale et al., 2022; Drozdov et al., 2015; Daglis et al., 2019; Li & Hudson, 2019; Su et al., 2014; Thorne et al., 2013; Tsurutani et al., 2020). Various observations of a growing peak of 1–2 MeV electron phase space density (PSD) at $L \simeq 4.5-5.5$ during prolonged disturbed periods suggest an important role of chorus-wave driven electron acceleration in this region outside the plasmasphere, often leading to high electron fluxes from 0.1 MeV up to ∼2 MeV (Allison et al., 2021; Boyd et al., 2018; Y. Chen et al., 2007; Green & Kivelson, 2004; Hua, Bortnik, & Ma, 2022; C. L. Tang et al., 2017; Turner et al., 2013).

Different methods have been developed for estimating maximum electron fluxes in the outer radiation belt. Empirical models provide estimates of maximum electron fluxes based on solar wind, storm, or substorm activity (Chu et al., 2021; Hua, Bortnik, Chu, Aryan, & Ma, 2022; Ma et al., 2022; Mourenas, Agapitov, et al., 2022; Mourenas et al., 2019; Simms et al., 2023). Theoretical or numerical models estimate upper limits on electron fluxes based on the consequences of chorus wave-particle interactions on electron fluxes. The two main theoretical approaches are (a) the Kennel-Petschek flux limiting mechanism, where wave-driven energy diffusion is implicitly neglected, and (b) numerical or analytical calculations including both wave-driven pitch-angle and energy diffusion, but which implicitly neglect the Kennel-Petschek flux limit (Horne et al., 2005; Hua, Bortnik, & Ma, 2022; Kennel & Petschek, 1966; Mourenas et al., 2018; Mourenas, Artemyev, et al., 2022; Olifer et al., 2021, 2022; Summers & Stone, 2022; Summers et al., 2002; Thorne et al., 2013; Zhang, Agapitov, et al., 2020; Zhang, Li,et al., 2021).

Linear and nonlinear chorus wave growth is expected to occur at magnetic latitudes $\lambda \lesssim 10°–15°$, leading to the formation of intense quasi-parallel lower-band (below half the gyrofrequency) chorus wave elements of mainly rising frequency (Nunn et al., 2021; Omura et al., 2008, 2009; Tao et al., 2011). At higher latitudes, both numerical simulations and spacecraft observations show that the superposition of various waves excited at the same or different times/locations, with different frequencies or wave-normal angles, leads to the formation of short chorus wave-packets (also called subpackets) with strong and random wave frequency and wave phase jumps between and sometimes within wave-packets (Mourenas, Zhang, et al., 2022; Nunn et al., 2021; Zhang

et al., 2018; Zhang, Agapitov, et al., 2020; Zhang, Demekhov, et al., 2021; Zhang, Mourenas, et al., 2020). The simultaneous waves are sufficiently intense and proximate in frequency to nearly satisfy the Chirikov criterion of resonance overlap (Mourenas, Zhang, et al., 2022; Nunn et al., 2021; Shapiro & Sagdeev, 1997; Tao et al., 2011). Since higher wave amplitudes would lead to resonance overlap and a stochastization of electron motion (Mourenas, Zhang, et al., 2022), these wave-packets cannot further grow nonlinearly by a significant amount, while increasing geomagnetic field inhomogeneity further increases stochastic electron motion at higher latitudes (Albert, 1993; Shklyar, 1981). This corresponds to a resonant wave-particle interaction regime close to quasi-linear diffusion (Allanson et al., 2020; Z. An et al., 2022; Artemyev et al., 2022; Gan et al., 2022; Mourenas et al., 2021; Mourenas, Zhang, et al., 2022; Zhang, Agapitov, et al., 2020).

In their pioneering work, Kennel and Petschek (1966) used quasi-linear diffusion theory to investigate interactions between electrons and whistler-mode waves. Neglecting wave-driven electron energy diffusion compared with pitch-angle diffusion, Kennel and Petscheck have shown that the trapped electron flux can be self-consistently maintained close to a stationary upper limit by electron loss into the atmosphere driven by whistler-mode waves generated at the magnetic equator by this same electron flux, corresponding to a regime of marginal stability for the waves (Kennel & Petschek, 1966). The Kennel-Petschek flux limit has been widely used ever since, either for predicting the highest electron fluxes in planetary radiation belts, or for comparisons with measured electron fluxes, demonstrating a good agreement at ∼100–300 keV and McIlwain shells $L > 4$ in the Earth's outer radiation belt, as well as some occasional apparent agreements (albeit more rough) up to ∼0.8–2 MeV (Kennel & Petschek, 1966; Mauk & Fox, 2010; Olifer et al., 2021, 2022; Schulz & Davidson, 1988; Summers et al., 2009). However, it is worth emphasizing that energy diffusion was explicitly neglected in the original work from Kennel and Petschek (1966), which focused on very low frequency plasmaspheric hiss whistler-mode waves.

Here, we first provide in Section 2 a brief overview of the Kennel-Petschek mechanism and its key assumptions. After this contextualization, we focus in the remainder of the paper on the second theoretical approach. We derive in Section 3 novel approximate analytical formulas for the steady-state electron energy distribution resulting from both chorus wave-driven electron energization and precipitation loss, valid over a much wider parameter domain than previous expressions (Mourenas, Artemyev, et al., 2022). In Section 4, the results obtained in Section 3 are used to provide approximate analytical estimates of the equilibrium upper limit on trapped electron flux from ∼0.1 to ∼1 MeV, taking into account both chorus wave-driven pitch-angle/energy diffusion and the strength of energetic electron injections from the plasma sheet. Finally, the obtained upper limits are compared in Section 5 with the maximum electron fluxes measured during various events of strong injections and chorus wave-driven electron acceleration in the Earth's outer radiation belt.

2. The Kennel-Petschek Flux Limit: A Brief Overview

2.1. Model and Assumptions

The Kennel-Petschek flux limitation mechanism (Kennel & Petschek, 1966) usually requires a wave power convective linear gain $G = \int 2\gamma_i \, ds/v_g = G_0 = 3$ over a distance $\Delta s \sim L\,R_E/2$ (with γ_i the linear wave growth rate, v_g the wave parallel group velocity and R_E the Earth's radius) to provide a wave power increase by a factor of 20 from a background noise level, deemed sufficient to produce a strong wave-driven diffusive electron precipitation into the atmosphere resulting in a self-limitation of the trapped electron flux (Mauk & Fox, 2010; Summers et al., 2009; Summers & Shi, 2014). However, recent spacecraft statistics of chorus waves (Agapitov et al., 2018) and simulations of chorus wave growth (Nunn et al., 2021; Omura et al., 2009; Tao et al., 2021) suggest that wave growth usually ends around magnetic latitudes $\lambda \sim 10°$, probably due to magnetic field inhomogeneity and Landau damping (Agapitov et al., 2018; L. Chen et al., 2013; Omura, 2021). Accordingly, a more realistic distance of convective wave growth is $\Delta s \approx LR_E/4$, or $\Delta\lambda \approx 15°$, including some wave growth upstream from the equator (Nogi & Omura, 2023; Tao et al., 2021).

But while the original Kennel-Petschek model assumed a linear wave growth (Kennel & Petschek, 1966), it was later recognized that whistler-mode chorus waves actually grow nonlinearly (Demekhov & Trakhtengerts, 2008; Nunn, 1974; Omura, 2021; Omura et al., 2008, 2013; Summers et al., 2011; Tao et al., 2020). After an initial stage of linear growth and as soon as the wave amplitude becomes sufficiently high to trap electrons, nonlinear wave growth takes place through the formation of resonant currents by phase space organization of resonant electrons, generating characteristic rising frequency elements (Karpman et al., 1974; Nogi & Omura, 2023; Nunn, 1974;

Omura, 2021; Omura et al., 2008). Near the equator, the wave amplitude should not significantly exceed the so-called *optimum amplitude* $B_{w,opt}$ maximizing nonlinear growth, of the order of $B_{w,opt} \sim 10^{-3}B_0 \approx 250$ pT, with B_0 the background magnetic field strength (Katoh et al., 2018; Omura & Nunn, 2011). But chorus waves can further grow nonlinearly through convective growth at higher latitudes (Omura et al., 2008, 2009; Summers et al., 2011), reaching maximum amplitudes $B_w \sim 2-3$ nT in spacecraft statistics (Zhang et al., 2019).

Taking into account that chorus waves actually grow with a nonlinear growth rate $\gamma_{nl,i}$ roughly ~2 to ~3 times larger than γ_i (Shklyar & Matsumoto, 2009; Summers et al., 2011), the required wave power gain $G_0 = 3$ (Summers et al., 2009) can probably be reached through nonlinear growth at latitudes $\lambda \lesssim 15°$. Near the loss-cone, the injected ~100 keV electrons can reach cyclotron resonance with chorus waves of typical frequency to equatorial gyrofrequency ratio $\omega/\Omega_{ce0} \sim 0.15-0.25$ at latitudes $\lambda \sim 10°–15°$ (Agapitov et al., 2018; Mourenas, Artemyev, Ripoll, et al., 2012). Therefore, the precipitation of ~100 keV electrons assumed in the Kennel-Petschek model must be produced by chorus waves having already reached the required gain G_0 at $\lambda \approx 10°$.

In the Kennel-Petschek model, it is further assumed that the trapped energetic electron distribution density n_{trap} adjusts itself to keep the wave gain G nearly constant at $G \sim G_0 = 3$, providing a quasi-stationary limiting flux $j_{KP} = (v/4)n_{trap,KP}$ (in e/cm^2/s), with v the average trapped electron velocity. The wave linear growth rate γ_i is proportional to n_{trap} for an assumed nearly constant temperature anisotropy s (for an electron distribution $f(\alpha_0) \sim \sin^{2s}\alpha_0$ with α_0 the equatorial pitch-angle) in the weak diffusion regime (Mauk & Fox, 2010; Summers et al., 2009; Summers & Shi, 2014). Therefore, if the flux j of trapped resonant electrons would increase above j_{KP}, the wave power B_w^2 would increase exponentially like $\sim\exp((j/j_{KP} - 1)G_0)$, leading to an exponentially faster electron loss through wave-driven pitch-angle scattering that would rapidly decrease the flux back to its limiting level j_{KP}. The exponential dependence of wave power on trapped flux j allows wave-driven electron precipitation into the atmosphere to balance the (varying) incoming flux of anisotropic electrons injected from the plasma sheet, establishing of a quasi-equilibrium trapped flux $j \simeq j_{KP}$.

Therefore, two key assumptions of the Kennel-Petschek flux limitation mechanism are: (a) the presence of a net electron loss due to electron precipitation into the atmosphere through quasi-linear pitch-angle electron diffusion by whistler-mode waves generated by the same electron population, and (b) an exponentially faster electron precipitation loss at higher electron flux due to the simultaneously increasing wave growth rate in the weak diffusion regime, preventing a significant flux increase above the upper flux limit j_{KP} (Kennel & Petschek, 1966; Summers et al., 2009).

As noted before, the assumption of a quasi-linear diffusive transport of electrons in phase space should be approximately justified for chorus waves, because they are sequentially generated by anisotropic electron populations injected from the plasma sheet in the form of mainly short wave packets, with strong amplitude modulations and fast and random jumps in frequency and phase limiting nonlinear transport (Allanson et al., 2020; Artemyev et al., 2021, 2022; Z. An et al., 2022; Gan et al., 2022; Tao et al., 2013; Zhang, Agapitov, et al., 2020; Zhang, Mourenas, et al., 2020). However, the characteristic time scale of diffusive electron loss into the atmosphere, the quasi-linear electron lifetime τ_L, cannot decrease below the strong diffusion lifetime τ_{SD}, which corresponds to a filled loss-cone in the strong diffusion regime (Kennel, 1969; Schulz, 1974a). In the strong diffusion regime, $\tau_L = \tau_{SD}$ is fixed and cannot decrease anymore when the electron flux and wave amplitude increase, while an expected reduction of the temperature anisotropy s by fast pitch-angle diffusion may also restrain wave growth, making the above assumption (b) invalid.

This led Etcheto et al. (1973) and Schulz (1974b) to infer that the Kennel-Petschek flux limit could be significantly exceeded in the strong diffusion regime. But these early works, like Kennel and Petschek (1966), focused on low frequency hiss waves with $\omega/\Omega_{ce0} \ll 0.1$, and explicitly neglected wave-driven electron energy diffusion, as appropriate in this case (Albert, 2005; Glauert & Horne, 2005). This is not justified anymore for high frequency chorus waves. Various works have demonstrated that chorus wave-driven electron energization can overcome wave-driven pitch-angle diffusion loss above $E \approx 100-300$ keV and rapidly increase the electron flux above its initial level at higher energy (Horne et al., 2005; Hua, Bortnik, & Ma, 2022; Mourenas, Artemyev, et al., 2022; Su et al., 2014; Summers et al., 2002; Thorne et al., 2013). This contradicts the above key assumption (a) of the Kennel-Petschek model, namely, the presence of a net electron loss allowing to maintain the trapped flux below an upper limit. On the other hand, a strong chorus wave-driven energy diffusion could maintain a significant temperature anisotropy s above ~100 keV even in the strong diffusion regime, by efficiently transporting lower-energy electrons to higher energies and higher pitch-angles $\alpha_0 > 50°$ (Horne et al., 2005; Su et al., 2014;

Summers et al., 2002; Yang et al., 2016). Energy diffusion can even transport electrons to energies higher than the maximum energy $E_{SD,max}$ of the strong diffusion regime, where $\tau_L(E) > \tau_{SD}(E)$ and the key assumption (b) is still valid, potentially extending the validity range of the Kennel-Petschek limit—until an eventual nonlinear saturation of the wave amplitude.

The energy spectrum $j_{KP}(E) \approx 1/E$ of the Kennel-Petschek flux limit has been calculated by assuming the same wave gain $G = G_0$ at all frequencies where $\gamma_i > 0$ (at $0 < \omega/\Omega_{ce0} < s/(1+s)$), integrating G over all resonant electrons (Mauk & Fox, 2010; Schulz & Davidson, 1988; Summers & Shi, 2014). At high energy $E > 1$ MeV, a high convective gain G could in principle be attained for not too high $j_{KP}(E)$ because a higher resonant parallel electron momentum $p_\parallel$ corresponds to a lower ω and to a lower v_g that may compensate the reduced γ_i (Summers & Shi, 2014), also allowing low-frequency waves to reach cyclotron resonance with high energy electrons near the loss-cone at the same latitude as lower energy electrons with high-frequency waves (Mourenas, Artemyev, Ripoll, et al., 2012). Outside the plasmasphere, however, the background whistler-mode wave power is usually very small at $\omega/\Omega_{ce0} < 0.05$ (Agapitov et al., 2018; Li et al., 2016). This is likely due, in part, to the prevalence of nonlinear wave growth (Omura et al., 2009; Summers et al., 2011). The frequency of chorus waves increases during their nonlinear growth, forming rising tones such that most of the wave power is at frequencies $\omega/\Omega_{ce0} > \omega_m/\Omega_{ce0} + 0.04$, well above the frequency ω_m of maximum γ_i (Nogi & Omura, 2023; Summers et al., 2011). This should probably reduce the effective convective gain G (over a fixed latitudinal range) at $\omega/\Omega_{ce0} < 0.05$, raising $j_{KP}(E)$ at $E > 1$ MeV. Finally, the additional presence of electromagnetic ion cyclotron (EMIC) waves in a noon/duskside plume can reduce the electron flux at $E > 1$ MeV well below the Kennel-Petschek limit (Mourenas, Artemyev, et al., 2022; Mourenas et al., 2016, 2021; Summers & Ma, 2000).

2.1.1. Insights From Observations and Unanswered Questions

Various observations have suggested the presence of an upper limit on electron fluxes at ∼30−800 keV during storm times (Hua, Bortnik, & Ma, 2022; Mourenas, Artemyev, et al., 2022; Olifer et al., 2021, 2022; K. Zhang et al., 2021). This upper limit is roughly consistent with the Kennel-Petschek model of electron flux self-limitation over this whole energy range (Mauk & Fox, 2010; Olifer et al., 2021; Summers et al., 2009), although it is often close to the Kennel-Petschek limit only below ∼300 keV. However, since chorus wave-driven electron energization, neglected in the Kennel-Petschek model, may overcome wave-driven pitch-angle diffusion loss, Hua, Bortnik, and Ma (2022) have used numerical simulations incorporating both pitch-angle and energy diffusion, demonstrating for the first time the existence of an upper limit on electron acceleration by chorus waves that could account for the observed flux limitation from ∼0.1 to ∼2−4 MeV, depending on the electron flux level at the lower energy boundary, presumed fixed by injections. Analytical and numerical analyses, as well as comparisons with observations in 2003 and 2017–2019, have confirmed the existence of such asymptotic upper electron energy spectra above ∼0.3−0.5 MeV, which correspond to steady-state attractors for the system dynamics in the absence of Kennel-Petschek flux limitation in this high energy range, where the maximum flux is set by the maximum flux at the lower energy boundary together with the steady-state spectrum shape (Mourenas, Artemyev, et al., 2022).

Accordingly, an important and heretofore unanswered question is: Which of these two alternative flux limiting mechanisms is actually operating in the outer radiation belt? To answer this question, it would be useful to obtain simple analytical formulas for the upper flux limit and energy spectrum shape corresponding to the dynamical equilibrium with steady-state attractor discussed above, in a wide parameter range. This would allow comparisons with observations and with the Kennel-Petschek limit. This could also allow to assess the parameter range where each mechanism is dominant and how they may affect each other. To obtain this information, we first derive in Section 3 novel approximate analytical formulas for the steady-state electron energy distributions reached under the influence of both electron energization and precipitation loss driven by whistler-mode chorus waves, considerably extending the parameter domain where they are available compared with our previous work (Mourenas, Artemyev, et al., 2022). Next, these results are used in Section 4 to provide analytical estimates of the upper limit on electron fluxes at all energies, taking into account both pitch-angle and energy diffusion and the strength of energetic electron injections from the plasma sheet.

3. Analytical Steady-State Electron Distributions Produced by Chorus Wave-Driven Diffusive Electron Energization and Precipitation

Below, we investigate the evolution of the electron distribution function $F(E,\alpha_0) = A(E)f(p)/c^3 = (E+1/2)J(E,\alpha_0)/\left[c((E+1)E)^{1/2}\right]$ (Horne et al., 2005) under the influence of

resonant interactions with chorus waves at $L = 4.5$–6.5, with $A(E) \simeq ((E+1)E)^{1/2}(E+1/2)$. E is henceforth in MeV, $f(p)$ is the electron phase space density (PSD) with p the electron momentum, and J is the electron differential flux.

However, just like chorus wave-driven electron energy diffusion was neglected in Section 2, we neglect here the Kennel-Petschek flux limit. We focus on the main part of the electron population, at equatorial electron pitch-angles $\alpha_0 > 50°$ (Mourenas, Artemyev, Agapitov, Krasnoselskikh, & Li, 2014; Olifer et al., 2022; Thorne et al., 2013). We take into account separate pitch-angle and energy diffusion operators, omitting for simplicity mixed diffusion terms in the Fokker-Planck diffusion equation (Glauert & Horne, 2005). Mixed (energy and pitch-angle) diffusion may have significant effects on electron flux evolution (Albert, 2009), but it is weaker for realistic, wide statistical distributions of quasi-parallel lower-band chorus wave-normal angles and frequencies than for monochromatic waves (Albert, 2009). The observed chorus wave normal angles θ and frequencies can usually be modeled by Gaussian distributions of half-widths $\Delta\theta = 30°$ centered at $\theta = 0$ and $\Delta\omega/\omega \sim 0.35$ centered at ω, respectively (Agapitov et al., 2018). Numerical simulations with such realistic chorus wave-normal angle and frequency distributions have shown weak effects of mixed diffusion in the domain $\alpha_0 \approx 70°$ mainly considered here (Albert & Young, 2005).

Accordingly, for an electron flux initially mainly present at low energy (e.g., after a storm main phase dropout, see Murphy et al., 2018; Turner et al., 2013) and evolving under the influence of chorus wave-electron interactions alone, the full relativistic Fokker-Planck equation describing the dynamics of the distribution $F(E, \alpha_0 > 50°)$ can be approximated as (Horne et al., 2005):

$$\frac{\partial F}{\partial t} = \frac{\partial}{\partial E}\left[A(E)D_{EE}\frac{\partial}{\partial E}\left(\frac{F}{A(E)}\right)\right] - \frac{F}{\tau_L}, \tag{1}$$

where D_{EE} is the bounce-averaged and magnetic local time (MLT) averaged wave-driven energy diffusion rate of electrons, and τ_L is the electron lifetime, that is, the timescale of electron loss into the atmosphere through quasi-linear resonant pitch-angle diffusion by chorus waves toward the loss-cone (Albert, 2005; Glauert & Horne, 2005; Horne et al., 2005; Lyons, 1974; Mourenas, Artemyev, Agapitov, & Krasnoselskikh, 2012, 2014; Mourenas, Artemyev, et al., 2022; Summers et al., 1998, 2002; Summers & Stone, 2022).

For $30° < \alpha_0 \leq \alpha_{0,max}(E)$ and $E \sim 0.1$–0.3 MeV, an approximate analytical expression, validated by numerical simulations, for the bounce- and MLT-averaged energy diffusion rate of electrons is (Mourenas, Artemyev, Agapitov, & Krasnoselskikh, 2012):

$$\frac{D_{EE}}{E^2}\left[\mathrm{s}^{-1}\right] \approx \frac{B^2_{\mathrm{w,acc}}\Omega^{3/2}_{ce0}\omega^{1/2}_{acc}(E+1)^{1/2}}{440\,\Omega^3_{pe0,acc}(E+1/2)\,E^{3/2}}, \tag{2}$$

with $B^2_{w.acc}$ (in pT^2) and $\omega_{acc}/\Omega_{ce0}$ the wave power and normalized frequency at magnetic latitudes $\lambda < 10°$ of cyclotron resonance with accelerated high α_0 electrons in spacecraft statistics (Agapitov et al., 2018; Li et al., 2016), and $\Omega_{pe0,acc}/\Omega_{ce0}$ the equatorial plasma frequency to gyrofrequency ratio, which determines the magnitude of D_{EE} (Agapitov et al., 2019; Summers et al., 1998). Cyclotron resonance is available only at $\alpha_0 \leq \alpha_{0,max}$, with $\cos\alpha_{0,max} \simeq |1-\gamma\omega/\Omega_{ce0}|(\Omega_{ce0}/\omega - 1)^{1/2}\Omega_{ce0}/\left[\Omega_{pe0}\left(\gamma^2-1\right)^{1/2}\right]$, and $\gamma = 1 + 2E$ the relativistic Lorentz factor (Mourenas, Artemyev, Ripoll, et al., 2012). In Equations 1 and 2, we use $D_{EE} = D_{EE}(\alpha_0 \sim 70°)$, an approximation which is justified since we focus on the main population of electrons located at $\alpha_0 > 50°$ (Mourenas, Artemyev, Agapitov, Krasnoselskikh, & Li, 2014; Olifer et al., 2022; Thorne et al., 2013), where D_{EE} merely varies like $\sin\alpha_0$ (Mourenas, Artemyev, Agapitov, & Krasnoselskikh, 2012). We further require that cyclotron resonance with electrons at the minimum energy be available up to $\alpha_{0,max} > 60°$ near the equator, so that most electrons can be diffused by chorus waves (since $\alpha_{0,max}(E)$ increases with E). This requirement is satisfied for a minimum energy ~0.1 MeV and typical parameters at $L = 4.5$–6.6 outside the plasmasphere, with $\Omega_{pe0,acc}/\Omega_{ce0} \gtrsim 4$ (Agapitov et al., 2019; Sheeley et al., 2001) and a gaussian distribution of chorus wave frequency with average frequency $\omega_{acc}/\Omega_{ce0} \sim 0.20$–$0.25$ and half-width $\Delta\omega/\omega \sim 0.35$ near the magnetic equator in spacecraft statistics (Agapitov et al., 2018; Li et al., 2016).

For $E \sim 0.1$–0.3 MeV, an approximate analytical expression, validated by numerical simulations, of the electron lifetime τ_L is (Artemyev et al., 2013; Mourenas, Artemyev, Ripoll, et al., 2012):

$$\frac{1}{\tau_L}\left[\mathrm{s}^{-1}\right] \approx \frac{B^2_{w,loss}\,\Omega^{4/3}_{ce0}}{1400\,\Omega^{14/9}_{pe0,loss}\,\omega^{7/9}_{loss}(2E+1)(E^2+E)^{7/9}}, \tag{3}$$

for a plasma frequency to gyrofrequency ratio $\Omega_{pe0,loss}/\Omega_{ce0} \geq 4$, with $B^2_{w,loss}$ in pT^2 and $\omega_{loss}/\Omega_{ce0} \sim 0.10$–$0.15$ the wave power and normalized frequency at magnetic latitudes $\lambda \sim 15°$–$25°$ of cyclotron resonance with such electrons near the loss-cone (Agapitov et al., 2018; Agapitov et al., 2019; Mourenas et al., 2021; Mourenas, Zhang, et al., 2022). Note that the right hand sides of Equations 2 and 3 are both averaged over MLT, as required for calculating diffusion over timescales longer than an azimuthal drift period of electrons around the Earth. The lifetime estimate in Equation 3 is valid for electrons up to $\alpha_0 \sim 85°$–$90°$, thanks to additional pitch-angle scattering via cyclotron and Landau resonance by lower-amplitude chorus waves of higher frequency at $\lambda < 6°$ (Agapitov et al., 2018; Hua, Bortnik, & Ma, 2022; Meredith et al., 2020; Ni et al., 2014; Yang et al., 2016), allowing most electrons to be scattered into the loss-cone (Albert & Shprits, 2009; Artemyev et al., 2013).

Based on Equations 2 and 3, we have $1/\tau_L \simeq \epsilon\, D_{EE}(1\text{ MeV})3/(2^{3/2}[E+1/2][E(E+1)]^{3/4})$, with $\epsilon = 2^{5/4}E^2/(D_{EE}\tau_L)$ an important normalization factor, calculated for simplicity at $E = 1$ MeV (Aryan et al., 2020; Mourenas, Artemyev, Agapitov, & Krasnoselskikh, 2012, 2014; Mourenas, Artemyev, et al., 2022). This gives a scaling $\tau_L D_{EE}/E^2 \sim (E+1)^{5/4}/E^{3/4}$. The crucial factor ϵ defines the regime of electron energization: with negligible electron loss when $\epsilon \ll 1$, and with important electron loss when $\epsilon \geq 1$.

During disturbed conditions with $Kp \in [3, 6]$ or $AE \in [400, 600]$ nT, Van Allen Probes statistics of plasma density and background magnetic field during chorus wave observations give an average ratio $\Omega_{pe0}/\Omega_{ce0} \simeq 4$ at $L \approx 5$ (Agapitov et al., 2019), while the normalized average chorus wave frequency is approximately $\omega_{acc}/\Omega_{ce0} \sim 0.2$ at $\lambda = 0°$–$10°$ (Agapitov et al., 2018; Li et al., 2016) and $\omega_{loss}/\Omega_{ce0} \lesssim 0.15$ at higher latitudes of cyclotron resonance with electrons of energy $E \geq 0.1$ MeV near the loss-cone (Agapitov et al., 2018). The latitudinal variation of plasma density needed to evaluate the latitude of resonance is given by an empirical model (Denton et al., 2006). Using these different parameters in Equations 2 and 3, one finds

$$\epsilon \;\approx\; 12 \cdot \max\left[0.08, \left(\frac{0.06}{E + 6\,E^5}\right)^{1/2}\right] \cdot \left(1 + 5.5\tanh\left(\frac{1}{60\,E^2}\right)\right) \tag{4}$$

at $L \approx 5$ for $E \in [0.1, 3]$ MeV during disturbed periods with electron injections. The middle term in Equation 4 is the average chorus wave power ratio $B^2_{w,loss}/B^2_{w,acc}$ during disturbed conditions with $Kp \sim 4$–5 based on Van Allen Probes and Cluster spacecraft statistics at $L \simeq 5$–6 (Agapitov et al., 2018). This ratio is roughly similar to the empirical ratio used by Hua, Bortnik, and Ma (2022). The last term in Equation 4, which increases by a factor of ~5 from 1 to 0.1 MeV, is used to recover full numerical calculations of $D_{EE}\tau_L$ (Artemyev et al., 2013; Mourenas, Artemyev, Agapitov, & Krasnoselskikh, 2012). Equation 4 gives ϵ values varying from ~50 to ~1 from low to high energy, in agreement with previous calculations for $E \approx 1$ MeV (Agapitov et al., 2019; Mourenas, Artemyev, et al., 2022).

The general steady-state solution to Equation 1, corresponding to $\partial F/\partial t = 0$, was shown by Mourenas, Artemyev, et al. (2022) to satisfy the following equation:

$$\left(\frac{1 + 4\left(E^2 + E\right)}{4(E^2 + E)^2} + 8 - \frac{\epsilon(1+2E)^2}{(E^2+E)^{5/4}}\right)F + (1+2E)^2\frac{\partial^2 F}{\partial E^2} - 4(1+2E)\frac{\partial F}{\partial E} = 0. \tag{5}$$

Mourenas, Artemyev, et al. (2022) remarked that the full Equation 5 is too complex to get a simple analytical solution valid for all E and ϵ values and, therefore, focused on high energies $E > 0.3$ MeV and small $\epsilon \leq 1$, corresponding to very active periods, to derive approximate *continuous* steady-state solutions $F_{st}(E)$ in this limited parameter range. In the present work, however, we are interested in the much wider parameter range $\epsilon \in [0.5, 50]$ for $E \in [0.1, 2]$ MeV. To obtain an analytically solvable equation, we therefore use two approximations, $(1+2E)^2/\left(E^2+E\right)^{5/4} \simeq K/(1+2E)^2$ with $K = 20 + 13\,E^2 + 0.06/E^2$ and $\left(1 + 4E^2 + 4E\right)/\left(2E^2 + 2E\right)^2 \simeq R/(1+2E)^2$ with $R = 4 + 1/E^{3/2}$, with less than ~16% error over 0.1–2 MeV. These approximations allow us to rewrite Equation 5 as

$$\left(8 - \frac{(\epsilon\,K - R)}{(1+2E)^2}\right)F + (1+2E)^2\frac{\partial^2 F}{\partial E^2} - 4(1+2E)\frac{\partial F}{\partial E} = 0, \tag{6}$$

with less than 5%–25% error on the first term over 0.1–2 MeV for $\epsilon \in [0.5, 50]$. Equation 6 has an exact analytical solution, provided that $(\epsilon K - R)$ is locally roughly constant, for instance inside each narrow energy bin of size $\Delta E \ll 0.1$ MeV. As a result, the steady-state electron distribution $F_{st}(E)$ is approximately given by

$$F_{st}(E) = (1+2E)^{3/2}\left(a \cdot I_{\frac{1}{2}}\left(\frac{\sqrt{\epsilon\,K - R}}{4E+2}\right) + b \cdot I_{-\frac{1}{2}}\left(\frac{\sqrt{\epsilon\,K - R}}{4E+2}\right)\right), \tag{7}$$

with $I_z(y)$ the modified Bessel function of the first kind, a and b two constants such that $F_{st}(E) > 0$, $K = 20 + 13\,E^2 + 0.06/E^2$, and $R = 4 + 1/E^{3/2}$. Equation 7 with positive or null constants a and b is valid for $\epsilon \in [0.5, 50]$ when $E \in [0.1, 2]$ MeV. Note that $(\epsilon K - R)$ is usually non-constant. In such a case, the steady-state distribution $F_{st}(E)$ from Equation 7 is a *discontinuous* solution to Equation 5 and it is approximately correct only inside one narrow energy bin ΔE at a time. Then, $F_{st}(E)$ must be normalized at the start of each energy bin centered at $E_{i+1} = E_i + \Delta E$ using a continuity equation $F_{st,i+1}(E_{i+1} - \Delta E/2) = F_{st,i}(E_i + \Delta E/2)$, and fixed values of $K(E_i)$, $R(\epsilon(E_i))$, and $\epsilon(E_i)$ must be used over each energy bin ΔE to calculate the variation of $F_{st}(E)$.

In practice, we only consider the steady-state electron distribution with $b = 0$ in Equation 7, because it increases much less, or decreases faster, toward higher E than the solution with $a = 0$. Therefore, it will be the first steady state reached from below when electron fluxes rise from low initial levels at $E > 0.3$–0.5 MeV during periods of strong chorus wave-driven electron energization (Hua, Bortnik, & Ma, 2022; Mourenas, Artemyev, et al., 2022; Olifer et al., 2021; Thorne et al., 2013). Even in the case of a high initial flux at high energy, the electron flux should also tend toward this lower steady-state solution, because reaching the upper one would require unrealistically strong injections at high energy (Mourenas, Artemyev, et al., 2022).

An alternative way to tackle Equation 5 is to assume that, for each ϵ value, the steady-state electron distribution has a simple form $F_{st}(E) = (1 + 2E)^x$ inside each energy bin of size ΔE centered at E, further assuming that its exponent x varies weakly with E for a sufficiently narrow energy bin ΔE. However, this last requirement is often less well satisfied than the requirement of a nearly constant $(\epsilon K - R)$ inside each energy bin used to derive Equation 7. Therefore, this alternative approach should provide *discontinuous* steady-state electron distributions $F_{st}(E)$ slightly less accurate than Equation 7. Such alternative solutions remain interesting and useful, though, because their simpler form allows an easier inspection of the system dynamics in their vicinity. Now, Equation 5 is transformed into a standard quadratic equation for x:

$$\left[16\left(E^2+E\right)^2\right]x^2 - \left[48\left(E^2+E\right)^2\right]x + 1 + 4E + 36\,E^2 + 64\,E^3 + 32\,E^4 - 4\,\epsilon\left(E^2+E\right)^{3/4}(2E+1)^2 = 0. \tag{8}$$

When the discriminant of quadratic Equation 8 is both positive and finite (>1), there are two solutions, $x_1(E)$ and $x_2(E)$, at each energy E. If $x_1(E)$ and $x_2(E)$ vary not too fast with E, they should correspond to approximate *discontinuous* steady-state distributions $F_{st}(E) = (1 + 2E)^{x_1}$ and $F_{st}(E) = (1 + 2E)^{x_2}$ relatively close to the *continuous* steady-state distributions $F_{st}(E)$ that are exact solutions to Equation 5. In the corresponding parameter range, E[MeV] > min[0.2/ϵ, 1], $\epsilon \geq 0$, and $E \in [0.1, 5]$ MeV, these two first-order solutions x_1 and x_2 are given by:

$$x_{1(2)} = \frac{3}{2} - (+)\frac{\sqrt{4(E^2(2+E)-1)E - 1 + 4\epsilon\left(E^2+E\right)^{3/4}(2E+1)^2}}{4\left(E^2+E\right)}. \tag{9}$$

In a limited parameter range such that $\epsilon \in [0, 1]$ and $E \in [0.1, 5]$ MeV, approximate analytical solutions x_1 and x_2 have already been obtained for *continuous* steady-state distributions of the same generic form $F_{st}(E) = (1 + 2x)^x$ (Mourenas, Artemyev, et al., 2022), with x_1 and x_2 given by:

$$x_{1(2)} = \frac{3}{2} - (+)\sqrt{\frac{3}{16} + \frac{10\,\epsilon^2}{9}}. \tag{10}$$

The solutions in Equation 9 are close to solutions in Equation 10 in the domain $E \sim 1$ MeV and $\epsilon = 1$ where they both exist. The corresponding first-order steady-state distributions have a form

$$F_{st}(E) = a \cdot (1 + 2E)^{x_1} + b \cdot (1 + 2E)^{x_2}, \tag{11}$$

with a and b two constants such that $F_{st}(E) > 0$ for all E.

Figure 1a shows the temporal evolution of the electron distribution $F(E, t)$ (in black) obtained by numerically solving Equation 1 for $\epsilon(E)$ given by Equation 4. A second-order fully implicit difference scheme and a tridiagonal matrix algorithm method are used to solve Equation 1, with a fixed boundary condition $F(E_0, t) = F(E_0, t = 0) = 1$ at a minimum energy $E_0 = 0.1$ MeV, corresponding to sustained low-energy injections, and an initial Dirac-like $F(E, t = 0)$ null above E_0. Chorus wave-driven electron energy diffusion leads to a fast increase of $F(E,$

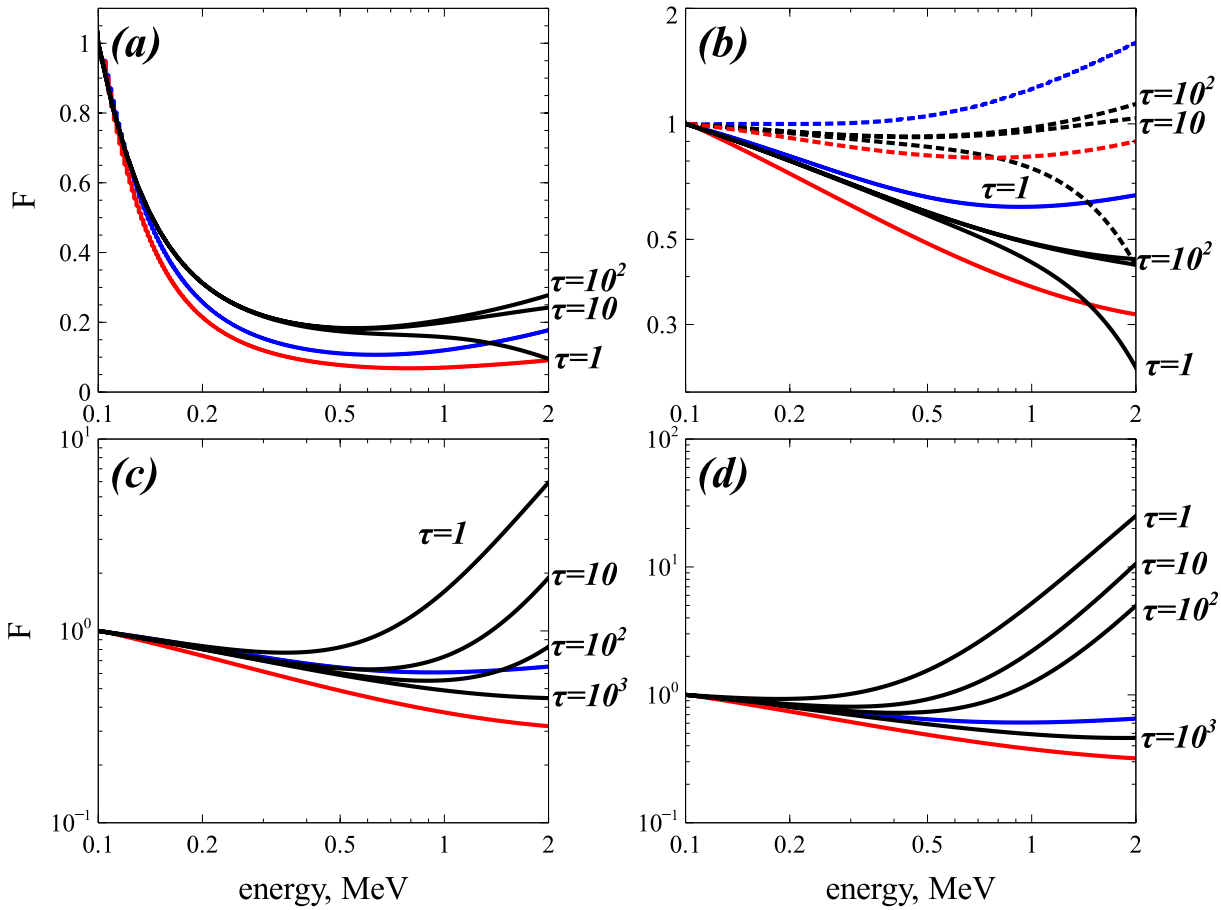

Figure 1. (a) Electron distribution $F(E, t)$ resulting from numerical solution of Fokker-Planck Equation 1 using $\epsilon(E)$ from Equation 4, with fixed boundary conditions $F(E_0, t) = 1$ at $E_0 = 0.1$ MeV and $F(E_{max}) = 0$ at upper boundary $E_{max} = 100$ MeV, and initially $F(E, t = 0) = 0$ at $E > E_0$ (in black). The approximate analytical steady-state distributions $F_{st}(E)$ given by Equations 9–11 or Equation 7 with $b = 0$ are shown (in red and blue, respectively), normalized to $F(E_0)$ from simulations. The dimensionless time is $\tau = t \cdot \left(D_{EE}/E^2\right)|_{1\,\mathrm{MeV}}$. (b) Same as (a) for a constant $\epsilon = 4$ (solid curves) or $\epsilon = 2$ (dashed curves). (c) Same as (b) for $\epsilon = 4$ and an initial $F(E, t = 0) \sim (1 + 2E)^x$ with $x = 3/2$ such that $x_1 < x < x_2$. (d) Same as (c) for an initial $F(E, t = 0) \sim (1 + 2E)\left(E^2 + E\right)^{1/2}$ corresponding to a flat electron PSD $f(E, t = 0) = \mathrm{const}$ and an initial $x > x_2$.

t) at $E > E_0$, until the electron distribution reaches a steady state at a normalized time $\tau = t \cdot \left(D_{EE}/E^2\right)|_{1\,\mathrm{MeV}} \approx 10$ (100) below 1 (2) MeV, corresponding to a balance between chorus-driven energization and loss. Figure 1a shows that the first-order analytical steady-state distribution $F_{st}(E) = a \cdot (1 + 2E)^{x_1}$ (in red) from Equations 9 and 11 is in rough agreement with the actual asymptotic steady-state electron distribution from the simulation (in black), with a very similar shape starting by a steep decrease at 0.1 MeV before a slower increase above 0.7 MeV, and a maximum discrepancy of a factor of ~2.5 at high energy. The difference with the asymptotic steady state from simulations is reduced to less than 35% in the case of a constant $\epsilon = 2$ or $\epsilon = 4$ in Figure 1b.

Figures 1a and 1b further show that the approximate analytical steady-state electron distribution $F_{st}(E)$ from Equation 7 with $b = 0$ (in blue) is in good agreement with actual steady-state distributions from simulations in all three cases, with a discrepancy always smaller than ~35%. The maximum discrepancy is twice smaller than for $F_{st}(E)$ from Equations 9 and 11 in Figure 1a. The difference between approximate and real steady-state distributions is due to the finite variation of x_1 and $(\epsilon K - R)$ with E, whereas these parameters were supposed constant for the derivation of Equations 7 and 9.

An advantage of the novel approximate analytical steady-state distributions provided in Equation 7 or in Equations 9 and 11, compared to previous ones in Equations 10 and 11 (Mourenas, Artemyev, et al., 2022), is their applicability over a much wider parameter range, including domains corresponding to realistic $\partial F_{st}/\partial E < 0$ at $\epsilon > \sqrt{2}$, which are encountered at low energy $E \sim 0.1$–0.5 MeV in Figure 1a.

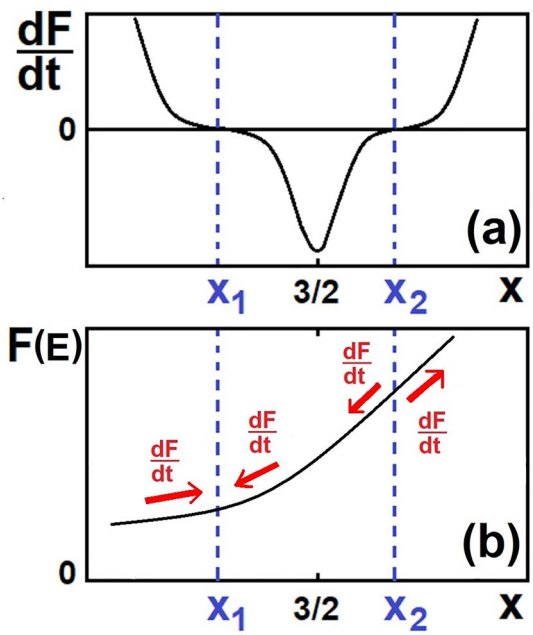

Figure 2. (a) Schematic view of the variation of $\partial F(E)/\partial t$ as a function of exponent x, for an electron distribution of the form $F(E) = (1 + 2E)^x$ in the diffusion Equation 1, where x_1 and x_2, given by Equation 9, correspond to two steady-state electron distributions with $\partial F(E)/\partial t = 0$. (b) Schematic view of $F(E) = (1 + 2E)^x$ and of the local trends (red arrows) for the evolution of $F(E, t)$, corresponding to the derivative $\partial F(E)/\partial t$ shown in panel (a), as a function of x.

In addition, Figures 2a and 2b show that substituting a distribution of the form $F(E) = (1 + 2E)^x$ (i.e., with fixed $F(E)$ at low $E < 0.1$ MeV) in Equation 1 gives a positive (negative) $\partial F(E)/\partial t$ for $x < x_1$ ($x > x_1$), which should lead x to progressively approach x_1. This suggests that the steady-state solution $F_{st}(E) = a \cdot (1 + 2E)^{x_1}$ with $a > 0$ and x_1 given by Equation 9 is an attractor for the system dynamics (Lichtenberg & Lieberman, 1983). Conversely, the solution $F_{st}(E) = b \cdot (1 + 2E)^{x_2}$ with $b > 0$ and x_2 given by Equation 9 is an unstable steady state, because $\partial F(E)/\partial t$ is negative (positive) for $x < x_2$ ($x > x_2$), which should result in a departure of x from x_2.

During its temporal evolution, however, the actual electron distribution $F(E, t)$ will not always have a local shape of the type $F(E) = (1 + 2E)^x$ at all energies. Therefore, additional numerical simulations have been performed to check the actual evolution of $F(E, t)$ for an initial shape $F(E, t = 0) = (1 + 2E)^x$ with $x > x_1$, adopting the same parameters as in Figure 1b (where initially $x < x_1$) with $\epsilon = 4$, except that we have initially $x_1 < x < x_2$ in Figure 1c and $x > x_2$ in Figure 1d. The simulations in Figure 1b–1d demonstrate that whatever the initial shape of $F(E, t)$, it tends toward a similar steady state $F_{st}(E)$ given by Equations 7 or 9–11 with $b = 0$. This is due to two facts: (a) a steeper electron PSD gradient leads to a stronger diffusive particle flow toward the region of lower PSD (Schulz & Lanzerotti, 1974), and (b) at a given energy, precipitation loss will decrease the PSD in the absence of a sufficient incoming flow of electrons produced by diffusive energization. Figures 1b and 1c therefore confirm that $\partial F/\partial t < 0$ when $x_2 > x > x_1$ and $\partial F/\partial t > 0$ when $x < x_1$, as expected from Figure 2.

Since the existence of steady-state solutions $F_{st}(E)$ may depend on the assumed form of the solution, another set of analytical steady-state solutions to Equation 5 has been derived, assuming a very different distribution form, $F_{st}(E) = a \cdot \left(E^2 + E\right)^x$, following the second approach discussed above and assuming again that x is not varying too fast with E. Equation 5 then becomes

$$1 + 4\left(E + E^2\right) + 32\left(E + E^2\right)^2 - 4\epsilon\left(E^2 + E\right)^{3/4}(1 + 2E)^2 + 4(1 + 2E)^4 x^2 - 4x(1 + 2E)^2\left(6E^2 + 6E + 1\right) = 0, \quad (12)$$

with solutions

$$x_{1(2)} = \frac{6\left(E^2 + E\right) + 1}{2(1 + 2E)^2} - (+)\frac{\sqrt{(E^2 + E)^2 + 2(E^2 + E) + \epsilon(E^2 + E)^{3/4}(2E + 1)^2}}{(1 + 2E)^2}, \quad (13)$$

with a first-order steady-state distribution of the form $F_{st}(E) = a \cdot \left(E^2 + E\right)^{x_1}$ when $E \in [0.05, 5]$ MeV and $\epsilon > -0.85$. The corresponding local approximate steady-state distributions $F_{st}(E)$ have a very similar shape as steady-state distributions $F_{st}(E) = a \cdot (1 + 2E)^{x_1}$ with x_1 from Equations 9–11 when $\epsilon \in [0, 25]$ or from Equation 10 when $\epsilon \in [0, 1]$. This indicates the robustness of these approximate first-order solutions.

However, for $\epsilon < -0.85$ we have $\partial F/\partial t > 0$ in Equation 1 for all exponents x of distributions of the form $F(E) \simeq (1 + 2E)^x$ or $F(E) \simeq \left(E^2 + E\right)^x$, suggesting that steady-state distributions are probably present only when $\epsilon > -1$. Another necessary condition for the existence of steady-state distributions $F_{st}(E)$ is a roughly constant $F(E_0, t) \sim \langle F(E_0, t)\rangle_t$ at some low energy $E_0 \leq E$ (Mourenas, Artemyev, et al., 2022) where cyclotron resonance with chorus waves is available up to $\alpha_0 > 50°$. Such a roughly constant $F(E_0)$ may be imposed by sustained electron injections from the plasma sheet (Hua, Bortnik, & Ma, 2022; Mourenas, Artemyev, et al., 2022), possibly with some help from the Kennel-Petschek flux limitation mechanism (Olifer et al., 2021; Summers et al., 2009). Significant (by ±50%) oscillations of $F(E_0, t)$ do not prevent the electron distribution from reaching a steady state (Mourenas, Artemyev, et al., 2022), but much stronger variations of $F(E_0, t)$ might prevent it.

Diffusive energization occurs progressively toward the region of lower electron PSD. Therefore, the maximum energy where the steady state is reached increases like the square root of time, as expected for a diffusive

broadening of the electron energy distribution (Balikhin et al., 2012; Mourenas, Artemyev, Agapitov, & Krasnoselskikh, 2014; Mourenas, Artemyev, et al., 2022).

4. Upper Flux Limits Based on Dynamical Equilibrium With Electron Injections and Pitch-Angle and Energy Diffusion

4.1. Generalities

It is worth noting that the steady-state distributions $F_{st}(E)$ derived in Section 3 only depend on ϵ (i.e., on the time-averaged $\langle D_{EE}\tau_L\rangle_t$) and on the level of the time-averaged $\langle F(E_0)\rangle_t$ at the low energy boundary E_0 (Bakhareva, 2003; Bakhareva, 2005; Hua, Bortnik, & Ma, 2022; Mourenas, Artemyev, et al., 2022). The local gradient $\partial f/\partial E$ self-adjusts and tunes the net incoming electron flow at energy E due to energy diffusion until it compensates electron loss due to pitch-angle diffusion. This is how the analytical steady-state electron distributions $F_{st}(E)$ found in Section 3 or in previous works (Bakhareva, 2003; Bakhareva, 2005; Mourenas, Artemyev, et al., 2022; Summers & Stone, 2022) can be reached in the outer radiation belt during prolonged periods of sustained injections and high chorus wave power (Mourenas, Artemyev, et al., 2022). Since net electron loss disappears once the steady-state shape $F_{st}(E)$ is reached, this may allow the whole distribution $F(E, t)$ to slowly increase afterward with $F(E_0, t)$ due to sustained injections, while roughly keeping its shape.

Consequently, the combination of chorus-driven pitch-angle and energy diffusion only impels the electron distribution to reach a steady state, $F_{st}(E)$, *of well-defined shape but arbitrary level* at $E \geq E_0$. It cannot enforce by itself an upper limit on the electron flux. The time-asymptotic equilibrium upper limit on $\langle F(E_0, t)\rangle_t$ has to be determined by a balance between the total quantity of electrons injected from the plasma sheet per second and the total amount of trapped electrons of all energies lost through precipitation per second (Etcheto et al., 1973). Accordingly, the system modeled by Equation 1 must be extended to take into account electron injections.

The energy range of electron injections usually mainly extends from $E_{\min} \approx 0.05$–0.1 MeV to $E_0 \approx 0.1$–0.3 MeV (Boyd et al., 2016; Runov et al., 2015; Turner et al., 2015). For the sake of simplicity, we assume that such energetic electron injections can be approximately modeled by an additional source term $S = +F_S(E)/\tau_S$ in Equation 1, with positive and constant (in time) $F_S(E)$ and τ_S (and $F_S(E)/\tau_S = 0$ at higher energy $E > E_0$). This yields a new diffusion equation instead of Equation 1:

$$\frac{\partial F(E)}{\partial t} = \frac{\partial}{\partial E}\left[A(E)D_{EE}\frac{\partial}{\partial E}\left(\frac{F(E)}{A(E)}\right)\right] - \frac{F(E)}{\tau_L} + \frac{F_S(E)}{\tau_S}, \tag{14}$$

Time History of Events and Macroscale Interactions during Substorms (THEMIS) spacecraft statistics of energetic electrons transported within Dipolarizing Flux Bundles and injected at $L \sim 7$–8 show that their differential flux $J_S(E)$ has a typical shape $J_S(E) \sim 1/\left(E^2 + E\right)^{2.25}$ at 0.04–0.4 MeV (Runov et al., 2015), very similar to the differential flux shape of ∼0.1–0.3 MeV electrons measured by the Van Allen Probes at $L \sim 4.5$–5.0 at the start of strong enhancements of relativistic electron flux (Olifer et al., 2022). Accordingly, we assume a shape $F_S(E)/\tau_S \sim (1 + 2E)/\left(E^2 + E\right)^{2.75} \sim 1/E^3$ for injected electrons. We also adopt a high injection rate $F_S(E)/\tau_S \gg F(E, t = 0)/\tau_L$, leading to an initial increase of $F(E, t)$ from $E_{\min}$ to E_0 (Olifer et al., 2022).

Observations at $L = 5$–7 in the outer radiation belt show that electron injections often maintain a relatively flat electron PSD near $E_{\min} \sim 0.05$–0.1 MeV (Baker et al., 1979; Olifer et al., 2022), corresponding to a lower boundary condition $\partial f/\partial E \sim \partial^2 f/\partial E^2 \sim 0$. This gives a null energy diffusion at $E_{\min}$ in Equation 14, allowing an increase of $F(E_{\min}, t)$ that can be stopped only when $F(E_{\min}, t)/\tau_L$ reaches $\approx F_S(E_{\min})/\tau_S$. At $E > E_{\min}$, the situation is the same as in Section 3, except for the additional presence of a source term F_S/τ_S representing injections in Equation 14. With this additional term, steady-state solutions to Equation 14 are still approximately given by Equation 7 or Equations 9–11, except that ϵ must be replaced by $\epsilon^\star$, with

$$\frac{\epsilon^\star}{\epsilon} = 1 - \frac{\tau_L(E)}{\tau_S}\left[\frac{F_S(E)}{F(E)}\right]. \tag{15}$$

For $F_S(E)/\tau_S \gg F(E, t)/\tau_L$ during the initial stage of injections, Equation 15 gives $\epsilon^\star < -1$ for a realistic $\epsilon \gg 1$. Then, Equations 9–11 and 13, 14 with Equation 5 and ϵ replaced everywhere by $\epsilon^\star$ indicate that any distribution of the form $F(E) = a \cdot (1 + 2\mathrm{E})^x$ or $F(E) = a \cdot \left(E^2 + E\right)^x$ will be such that $\partial F/\partial t > 0$ in Equation 14, leading to a fast initial increase of $F(E, t)$ from $E_{\min}$ to E_0.

4.2. Moderately Strong Electron Injections

We first examine moderately strong electron injections corresponding to a regime of weak diffusion (Kennel, 1969). In the weak diffusion regime, one has $\tau_L > \tau_{SD}$ at $E \geq E_{\min}$, with $\tau_{SD} = 0.0194\, L^4(4-3/L)^{1/2}(1+2E)/\left[(1-\eta)\left(E^2+E\right)^{1/2}\right]$ s the minimum lifetime reached in the strong diffusion regime (Kennel, 1969; Schulz, 1974a) and $\eta(E)$ the albedo of the atmosphere. Simulations and observations suggest that typical values are $\eta \sim 0.8$ and $\eta \sim 0.4$ during weak and strong diffusion at ∼0.1 MeV and $L \sim 5$–6 (Marshall & Bortnik, 2018; Mourenas et al., 2021; Selesnick et al., 2004).

In a quasi-stationary regime, $\partial F/\partial t \simeq 0$, an estimate of the upper limit $F_{UL}(E)$ of the equilibrium trapped electron distribution $F(E, t)$ can then be derived. The conservation of the total number of trapped electrons requires a balance between the precipitation outflow and the injection inflow,

$$\int_{E_{\min}}^{+\infty} \frac{F_{UL}(E)}{\tau_L(E)}\, dE \;\approx\; \int_{E_{\min}}^{E_0} \frac{F_S(E)}{\tau_S}\, dE, \tag{16}$$

in order to prevent a further increase of the trapped electron flux. Note that the PSD $f(E)$ cannot assume an increasing slope with $\partial f/\partial E > 0$ without immediately stopping the inflow of electrons accelerated from lower energy. Therefore, it is the global level of $F(E)$ which must rise at all energies to satisfy Equation 16.

We henceforth focus on energies $E \geq E_{\min} = 0.1$ MeV and $E \leq 2$ MeV, corresponding to the validity range of Equation 4 when $Kp \sim 3$–6 or $AE \sim 400$–600 nT. As shown in Section 3, the equilibrium trapped electron distribution F_{UL} at $E \geq E_0$ will assume a steady-state attractor shape $F_{st}(E)$ given by Equation 7 with $b = 0$ and $\epsilon(E)$ from Equation 4. Thus, at E_0 we have $\epsilon^\star = \epsilon > 10$ and $\partial F_{UL}/\partial E < 0$. At $E_{\min}$, the lower boundary condition $\partial f/\partial E = \partial^2 f/\partial E^2 = 0$ gives $\partial F_{UL}/\partial E \sim 0$, roughly equivalent to $\epsilon^\star \approx 0$. For $E_{\min} < E < E_0$, the widening of the initial energy spectrum by electron energization implies that we should get $F_{UL}(E)/\tau_L < F_S(E)/\tau_S$, corresponding to $\epsilon^\star$ values ranging from <-1 to $\epsilon/2$. In this energy range, an equilibrium distribution can be imposed (even when $\epsilon^\star < -1$) by Equation 16 together with boundary conditions at $E_{\min}$ and E_0 and the necessity of keeping $\partial f/\partial E < 0$ to allow electron transport toward higher E through chorus-driven acceleration. Continuity and differentiability of $F_{UL}(E)$ at all E should then impose a smooth transition from $\epsilon^\star \sim \epsilon$ and $\partial F_{UL}/\partial E < 0$ at E_0 to $\epsilon^\star \approx 0$ and $\partial F_{UL}/\partial E \approx 0$ at $E_{\min}$. Note that a smaller $\epsilon^\star$ corresponds to a larger integral of $F_{UL}(E) \sim F_{st}(E)$ and a smaller $F_{UL}(E_{\min})$ in Equation 16. For the sake of simplicity and without loss of generality, we can therefore use $\epsilon^\star = \epsilon$ at all E to infer the maximum possible value of $F_{UL}(E_{\min})$. This should lead to only a slight overestimation of $F_{UL}(E_{\min})$ and of the decrease of $F_{UL}(E)$ from $E_{\min}$ to E_0 during events with $E_0 > 0.1$ MeV.

To estimate F_{UL}, we need to determine the maximum energy $E_{\max}(t)$ up to which $F(E, t)$ assumes the steady-state spectrum shape at a given time. For $\epsilon(E)$ given by Equation 4 during strong injections with $Kp > 4$, we have $E_{\max} \approx \left(6\, t D_{EE}|_{E_{\max}}\right)^{1/2}$ based on previous work for a Dirac-like instantaneous injection at $t = 0$ at low energy (Mourenas, Artemyev, Agapitov, & Krasnoselskikh, 2014; Mourenas, Artemyev, et al., 2022). Using D_{EE} from Equation 2 and normalizing this approximate theoretical relationship by a constant factor to recover full numerical results in the case of continuous injections at low energy when $\epsilon \in [1, 5]$ (Mourenas, Artemyev, et al., 2022), this gives

$$E_{\max}[\text{MeV}] \;\approx\; 0.25\,(6\, t\, D_{EE}|_{1\,\text{MeV}})^{0.56}, \tag{17}$$

valid for $E_{\max} \gtrsim 0.5$ MeV. Based on statistics from the Van Allen Probes and Cluster spacecraft near $L \approx 5$, the time- and MLT-averaged chorus wave power near the equator is $B^2_{w.acc} \approx (60)^2$ pT^2 when $Kp = 4$–6 (Agapitov et al., 2018), $\Omega_{pe0}/\Omega_{ce0} \simeq 4$ at $L \approx 5$ (Agapitov et al., 2019), and $\omega_{acc}/\Omega_{ce0} \sim 0.2$ at $\lambda = 0°$–10° (Agapitov et al., 2018; Li et al., 2016). For sustained electron injections lasting up to $t \approx 12$−72 hr (Agapitov et al., 2018; Hua, Bortnik, & Ma, 2022; Mourenas, Artemyev, et al., 2022; Turner et al., 2015), Equation 17 gives $E_{\max} \approx 0.8$–2 MeV. The weak variation of $E_{\max}$ with parameters in Equation 17, and the much smaller electron flux above ∼1.5 MeV during intense injections (Hua, Bortnik, & Ma, 2022; Mourenas, Artemyev, et al., 2022; Olifer et al., 2022), lend credence to this first-order estimate.

The equilibrium upper limit $F_{UL}(E)$ from $E_{\min}$ to $E_{\max}$ can be approximated by a local (in E) steady-state distribution from Equation 7 with $b = 0$ and $\epsilon(E)$ from Equation 4. Using $\tau_L(E)$ from Equation 3 multiplied by $\epsilon(E)^{-0.6}$ to

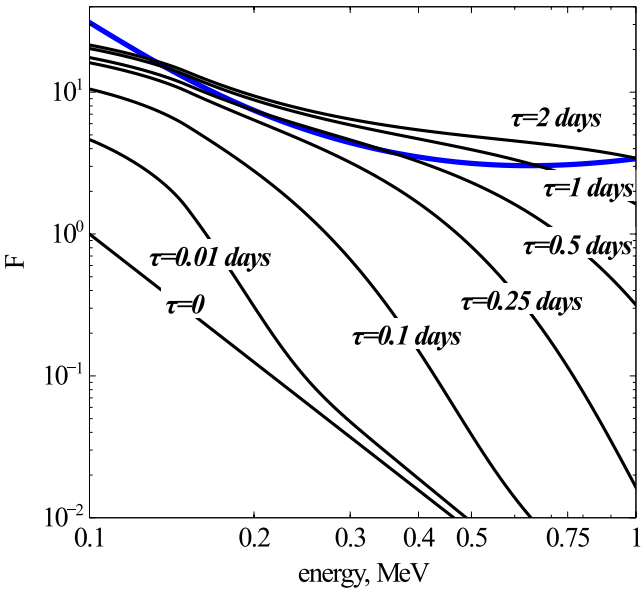

Figure 3. Evolution of the trapped electron distribution $F(E, t)$ (black curves), obtained by numerically solving Equation 14. We adopt a realistic $\left(D_{EE}/E^2\right)|_{1\,\mathrm{MeV}} = 0.25\,\mathrm{day}^{-1}$ for $Kp = 4$–6. We use $\epsilon(E)$ from Equation 4, a variation of $1/\tau_L$ with E as in Equation 3 multiplied by $(\epsilon(E)/\epsilon(1\,\mathrm{MeV}))^{0.6}$, and a variation of D_{EE}/E^2 with E as in Equation 2 multiplied by $(\epsilon(E)/\epsilon(1\,\mathrm{MeV}))^{-0.4}$, to take into account the latitudinal distribution of chorus wave power and exact numerical variations of τ_L and D_{EE} (Agapitov et al., 2018; Aryan et al., 2020). The lower boundary condition corresponds to $\partial f/\partial E = \partial^2 f/\partial E^2 = 0$ at $E_{\min} = 0.1$ MeV, $F(E_{\max}) = 0$ at $E_{\max} = 100$ MeV, and $F(E, t = 0) = (0.1/E)^3$. The injection source term is $F_S(E)/\tau_S = 1000F(E, t = 0)$ day^{-1} at $E \in [0.1$–$0.15]$ MeV. The analytical equilibrium upper limit $F_{UL}(E)$ given by Equation 20 using Equation 7 with $b = 0$ is shown (blue curve).

take into account the decrease of chorus wave power away from the equator (Agapitov et al., 2018), and $E_{\max}$ from Equation 17, a numerical integration of Equation 16 yields:

$$\frac{F_{UL}(E_{\min})}{\tau_L(E_{\min})}\left(\frac{5/3}{E_{\min}}\right)^{-6/5} \approx \int_{E_{\min}}^{E_0} \frac{F_S(E)}{\tau_S}\,dE \tag{18}$$

for $t > 6$ hr and $E_{\min} \in [0.1, 0.3]$ MeV. Using the typical shape $F_S(E)/\tau_S \sim 1/E^3$ of injected electrons (Runov et al., 2015) and assuming $E_0 > 1.5\,E_{\min}$, Equation 18 gives:

$$\frac{F_{UL}(E_{\min})}{\tau_L(E_{\min})} \approx \frac{F_S(E_{\min})}{\tau_S}\cdot\left(\frac{E_{\min}}{0.1}\right)^{-1/5}\cdot\left(\frac{E_0}{1.9\,E_{\min}}\right)^{1/2}, \tag{19}$$

valid at $L \approx 5$–6 when $Kp = 4$–6 for $E_{\min} \in [0.1, 0.3]$ MeV, $E_0/E_{\min} \in [1.5, 3]$, and $t > 6$ hr. The corresponding equilibrium upper limit at $E \geq E_{\min}$ is

$$F_{UL}(E) \approx F_{UL}(E_{\min})\cdot\frac{F_{st}(E)}{F_{st}(E_{\min})}, \tag{20}$$

with $F_{UL}(E_{\min})$ given by Equation 19 and $F_{st}(E)$ given by Equation 7 with $b = 0$ and $\epsilon(E)$ from Equation 4.

Figure 3 shows simulation results obtained by numerically solving Equation 14 in the case of a moderately strong low-energy electron injection modeled by a source term $F_S(E)/\tau_S = 1000F(E, t = 0)$ day^{-1} over 0.1–0.15 MeV with a realistic injection energy spectrum $F(E, t = 0) = (0.1/E)^3$ (Olifer et al., 2022; Runov et al., 2015). In this case, injections are initially much faster than precipitation loss. We adopt a simple but realistic lower boundary condition, such that $F(E_{\min}, t)$ is given by Equation 14 with $D_{EE} = 0$, equivalent to a condition $\partial f/\partial E = \partial^2 f/\partial E^2 = 0$ there. This lower boundary condition corresponds to injections maintaining a relatively flat electron PSD in the vicinity of $E_{\min} \approx 0.1$ MeV, as during several observations (Baker et al., 1979; Olifer et al., 2022). This allows a rapid increase of $F(E_{\min}, t)$ as long as $F(E_{\min}, t)/\tau_L < F_S(E_{\min})/\tau_S$. In addition, we use a realistic $\epsilon(E)$ given by Equation 4 and a realistic diffusion rate $\left(D_{EE}/E^2\right)|_{1\,\mathrm{MeV}} = 0.25\,\mathrm{day}^{-1}$ for $AE \sim 500$ nT or $Kp \sim 4$–5 at $L = 4.5$–7 (Agapitov et al., 2018, 2019).

Figure 3 shows that the trapped electron distribution $F(E, t)$ from the simulation (black curves) initially increases due to faster electron injection than loss (with $\epsilon^\star < -1$ and $\partial F/\partial t > 0$). After ~1 day to ~2 days, $F(E, t)$ reaches its equilibrium upper limit up to ~0.5 MeV to ~0.8 MeV. The equilibrium upper limit in the simulation (upper black curve) is in good agreement with the analytical estimate $F_{UL}(E)$ given by Equation 20 (blue curve) from 0.1 to 1 MeV, although it decreases less fast than $F_{UL}(E)$ from 0.1 to 0.15 MeV within the energy range of electron injections.

4.3. Extremely Strong Electron Injections

Let us now consider the case of *extremely strong injections*, such that $F_S(E)/\tau_S > F(E)/\tau_{SD}(E)$ over a finite energy range at $E \geq E_{\min}$. At the strong diffusion threshold, we have $D_{EE} = D_{EE}^{SD} = \left(E^2 + E\right)^{5/4}/(\epsilon\,\tau_{SD})$. But D_{EE} may increase above D_{EE}^{SD} during sufficiently strong injections of 10–300 keV electrons, due to a corresponding amplification of chorus wave power (Omura et al., 2008).

Strong substorms with $Kp \sim 5$–6 and $AE \sim 600$–1,000 nT usually correspond to a time- and MLT-averaged chorus wave power $\langle B_w^2\rangle_{t,MLT} \sim (50)^2$ pT^2 at latitudes $\lambda \sim 15°$ of cyclotron resonance with 100 keV electrons near the loss-cone at $L \sim 5$–6 (Agapitov et al., 2018). To reduce the lifetime τ_L to its minimum value, $\tau_{SD}(E_{\min}) \sim 140$ s, the average wave power must increase up to $\langle B_w^2\rangle_t \sim (280)^2$ pT^2, a level sometimes observed for hours at $L \sim 5$ during geomagnetic storms and substorms (Chakraborty et al., 2022; Elliott et al., 2022; C. Tang et al., 2023), or during microbursts (Zhang et al., 2022). Such large amplitudes can lead to electron trapping and nonlinear acceleration

(Katoh & Omura, 2007; Vainchtein et al., 2018; Zhang et al., 2019), but significant wave amplitude modulations and random phase jumps between and inside intense wave packets usually restore a diffusive-like electron transport that can be approximated by quasi-linear diffusion (Artemyev et al., 2021, 2022; Z. An et al., 2022; Tao et al., 2013; Zhang, Agapitov, et al., 2020; Zhang, Mourenas, et al., 2020).

In the case of extremely strong injections, the integral of $F_{UL}(E)$ in Equation 16 has to be performed by parts as:

$$\int_{E_{\min}}^{E_{SD,max}} \frac{F_{UL}(E)}{\tau_{SD}}\, dE + \int_{E_{SD,max}}^{E_{\max}} \frac{F_{UL}(E)}{\tau_L}\, dE \approx \int_{E_{\min}}^{E_0} \frac{F_S(E)}{\tau_S}\, dE, \tag{21}$$

with $E_{\max}$ given by Equation 17 and $F_S(E) \sim 1/E^3$ (Runov et al., 2015).

At $E < E_{SD,max}$, we have $\tau_L = \tau_{SD}$ but we should get $D_{EE} \gg D_{EE}^{SD}$ when chorus wave power at low latitudes reaches higher levels than for $D_{EE} = D_{EE}^{SD}$. In this situation, we can therefore use the approximations $\epsilon \approx 0$ and $\epsilon^\star \approx 0$ at $E \in [E_{\min}, E_{SD,max}]$, giving $F_{st}(E) = (\ln(E+1) - \ln(E))(1+2E)\left(E^2+E\right)^{1/2} \simeq 3\sqrt{E}$ for $E \in [0.06, 1.8]$ MeV (Mourenas, Artemyev, et al., 2022). At higher energy $E \in [E_{SD,max}, E_{\max}]$, ϵ is then also small ($\epsilon \approx 0$), allowing to use the same steady-state distribution $F_{st}(E)$, corresponding to a differential flux $J_{st}(E) \sim (1+E)^{1/2}E/(1+2E)$ increasing with energy.

The first integral of $F_{UL}(E)$ in Equation 21 can then be well approximated by power-law functions of $E_{SD,max}$ and $E_{\min}$ for $E_{\min} \in [0.1, 0.3]$ MeV, $E_{SD,max} \in [0.3, 2]$ MeV and $E_{SD,max} \geq E_{\min} + 0.2$. To estimate $E_{\max}$, we take into account the presence of intense EMIC waves in high-density plasmaspheric plume/boundary regions at dusk and $L \approx 5$ during strong injections with $AE > 500$ nT, contemporaneously with chorus waves in low-density regions at dawn (H. Chen et al., 2020; Ross et al., 2021; Zhang et al., 2016; Zhang et al., 2017), which should impose an upper limit $E_{\max} \approx 1$ MeV to elevated electron flux near $L = 5$ (Li et al., 2007; Mourenas et al., 2016, 2021; Mourenas, Artemyev, et al., 2022; Zhang et al., 2017). Adopting this value of $E_{\max}$, the second integral of $F_{UL}(E)$ can be similarly well approximated, giving

$$\left(\frac{E_{SD,max}^{9/5}}{3.3\ E_{\min}} + \frac{E_{SD,max}^{3/4}}{3\ E_{\min}^{3/4}}\right)\frac{F_{UL}(E_{\min})}{\tau_{SD}(E_{\min})} \approx \left(\frac{0.5\ E_{\min}}{1+E_{\min}}\right)\frac{F_S(E_{\min})}{\tau_S}, \tag{22}$$

with an equilibrium upper limit at $E \geq E_{\min}$ given by

$$F_{UL}(E) \simeq F_{UL}(E_{\min}) \cdot \sqrt{\frac{E}{E_{\min}}}, \tag{23}$$

where $F_{UL}(E_{\min})$ is given by Equation 22.

4.4. Variations With Parameters

The equilibrium upper limits F_{UL} derived in Sections 4.2 and 4.3 based on Equations 14 and 16 are valid for $E \gtrsim 100$ keV and $\Omega_{pe0}/\Omega_{ce0} \approx 4$ at $L \sim 5$–6 when $Kp > 4$. Strong Landau damping of chorus waves at $\omega/\Omega_{ce0} > 0.3$ (Agapitov et al., 2018; L. Chen et al., 2013) generated by ~20–40 keV electrons may prevent an efficient chorus wave-driven diffusion below ~50 keV. For $\Omega_{pe0}/\Omega_{ce0} < 3$ or >5, the value of ϵ given in Equation 4 for $\Omega_{pe0}/\Omega_{ce0} \approx 4$ should be rescaled by a factor $(\Omega_{pe0}/4\Omega_{ce0})^{3/2}$, also replacing the second term in Equation 4 by $\langle B_w^2(\lambda_{R,loss})\rangle_{MLT}/\langle B_w^2(\lambda_{R,acc})\rangle_{MLT}$, with $\lambda_{R,loss}$ and $\lambda_{R,acc}$ the latitudes of cyclotron resonance with electrons near the loss-cone and at $\alpha_0 > 45°$, respectively (Mourenas, Artemyev, et al., 2022), using a statistical model of chorus wave power latitudinal distribution (Agapitov et al., 2018; Meredith et al., 2020). Equations 2 and 3 should remain valid at $E \gtrsim 0.1(4\Omega_{ce0}/\Omega_{pe0})^2$ MeV. Note that ϵ is approximately proportional to the middle latitude to low latitude chorus wave power ratio and to $(\Omega_{pe0}/\Omega_{ce0})^{3/2}$. Therefore, a higher $\Omega_{pe0}/\Omega_{ce0}$ will increase $F_{UL}(E_{\min})$ and decrease $F_{UL}(E > E_{\min})/F_{UL}(E_{\min})$. In addition, a reduction of $F_{UL}(E)$ compared with the present estimates is likely above ~1.5 MeV during periods with $Kp > 4$–5, due to combined pitch-angle scattering by EMIC and chorus waves (Mourenas et al., 2016; Mourenas et al., 2021; Zhang et al., 2017).

4.5. Comparison With the Kennel-Petschek Flux Limit

It is instructive to compare the upper limit $F_{UL}(E)$ derived in Sections 4.2 and 4.3, based on a dynamical equilibrium in the presence of injections and both chorus wave-driven pitch-angle and energy diffusion, with the

classical Kennel-Petschek limit $F_{KP}(E)$ (Kennel & Petschek, 1966; Mauk & Fox, 2010; Summers et al., 2009; Summers & Shi, 2014). Both mechanisms rely on interactions between trapped electrons and whistler-mode chorus waves and require cyclotron resonance between chorus waves and electrons up to $\alpha_0 > 50°$ to enable the precipitation of a large part of the trapped electron population into the atmosphere. This requires a sufficiently high electron energy, such that $\left(E^2 + E\right) > 0.6\,(\Omega_{ce0}/\Omega_{pe0})^2(\Omega_{ce0}/\omega)(1 - \omega/\Omega_{ce0})(1 - (1 + 2E)\omega/\Omega_{ce0})^2$, with E in MeV. For such electrons, the actual upper limit at $E \geq E_{\min} \sim 0.1$ MeV may be imposed by the lowest of these two upper limits, depending on the strength F_S/τ_S of injections.

However, these two flux limiting mechanisms are different. The upper limit $F_{UL}(E)$, derived based on Equations 14 and 16, is fixed by an equilibrium between the total electron inflow from injections and the total electron outflow into the atmosphere, together with a fine-tuning of $\partial F_{UL}/\partial E$ allowing to reach a steady-state distribution shape $F_{UL}(E) \sim F_{st}(E)$ such that $\partial F_{UL}/\partial t = 0$ in the presence of both chorus wave-driven pitch-angle and energy diffusion. As emphasized in Section 2, the classical Kennel-Petschek flux limit relies on two different key assumptions: (a) a net electron loss at all E when $F(E, t) > F_{KP}(E)$, such that $\partial F(E, t)/\partial t < 0$, corresponding to electron precipitation into the atmosphere by chorus waves generated by the same electron population, and (b) an exponentially faster electron loss as $F(E, t)$ increases above $F_{KP}(E)$, due to the exponentially larger power B_w^2 of chorus waves generated by these trapped electrons, rapidly leading to an equilibrium between electron inflow from injections and electron outflow into the atmosphere at a level $F(E, t) \approx F_{KP}(E)$ that should depend only logarithmically on the strength F_S/τ_S of injections (Kennel & Petschek, 1966). The second assumption requires $\tau_L(E) > \tau_{SD}(E)$ to allow a decrease of $\tau_L(E)$ as $F(E, t)$ increases (Etcheto et al., 1973; Schulz, 1974b). The first assumption suggests that the Kennel-Petschek flux limit (which explicitly assumes $D_{EE} = 0$ at all E) could become inefficient at high energy, whenever chorus wave-driven energy diffusion leads to an increase of electron flux at this energy instead of a decrease (Horne et al., 2005; Hua, Bortnik, & Ma, 2022; Mourenas, Artemyev, et al., 2022; Summers et al., 2002).

Consequently, if $F_{UL}(E) < F_{KP}(E)$ at all $E \geq E_{\min}$, the actual upper limit to $F(E, t)$ should be $F_{UL}(E)$. Conversely, if $F_{KP}(E) < F_{UL}(E)$ from $E \sim E_{\min}$ to $E \sim E^\star < E_0$, then $F(E, t)$ should be capped at the Kennel-Petschek limit $\approx F_{KP}(E)$ in this low energy range. At higher energy $E > E_0$, although an increase of $F(E, t)$ above $F_{KP}(E)$ could exponentially increase chorus wave power B_w^2, both $1/\tau_L$ and D_{EE} would then increase similarly and ϵ would remain unchanged. Therefore, at $E > E_0$ the situation should remain the same as in Section 3: a finite chorus wave-driven energy diffusion (with $\epsilon > 0$) should lead $F(E, t)$ to assume a steady-state shape $\sim F_{st}(E) \sim F_{UL}(E)$, whatever the ratio $F_{UL}(E)/F_{KP}(E)$ there. However, the Kennel-Petschek limit at $E^\star < E_0$ would then represent an *anchor point* for the steady-state electron distribution at $E > E_0$, leading to an upper limit $\approx F_{UL}(E) \times F_{KP}(E^\star)/F_{UL}(E^\star)$.

In the future, the above conjectures could be checked in full numerical simulations including precisely both flux limiting mechanisms. Comparisons with observations may also allow to identify the mechanism at work during given events, provided that these two upper limits vary differently with parameters. As shown in Sections 3 and 4.2, the equilibrium upper limit $F_{UL}(E)$ depends on both the time-averaged injection rate F_S/τ_S and ϵ, while the corresponding energy spectrum mainly depends on ϵ. At $L \sim 5$–6 when $Kp > 4$, the steady-state energy spectrum $F_{UL}(E)$ is given approximately by Equation 7 with $b = 0$ and Equation 4, although $F_{UL}(E)$ can decrease more slowly from 0.1 to 0.2 MeV during strong injections extending up to ~0.15–0.2 MeV (e.g., see Figure 3). A higher $\Omega_{pe0}/\Omega_{ce0} > 4$ should amplify the decrease of $F_{UL}(E)$ from 0.1 to 0.6 MeV (see Section 4.4). The Kennel-Petschek limit $F_{KP}(E)$ depends on the electron temperature anisotropy s, energy E, and L, with a typical differential flux scaling $J_{KP} \sim 1/(s\,E^\beta\,L^4)$ (Olifer et al., 2022; Summers & Shi, 2014), corresponding to $F_{KP}(E) \sim (E + 1/2)/\left(E^\beta\left(E^2 + E\right)^{1/2}\right)$, with $\beta \sim 0.7$–0.9 and $s \sim 0.25$–0.35 at 0.1–0.6 MeV during sustained injections with $Kp > 4$ and $AE > 400$ nT near $L \approx 5$ (Olifer et al., 2022). A higher $\Omega_{pe0}/\Omega_{ce0} > 4$ should weaken the decrease of $F_{KP}(E)$ from 0.1 to 0.6 MeV (Summers & Shi, 2014).

For $F_{UL}(E_{\min}) = F_{KP}(E_{\min}) = F(E_{\min})$, with $F(E_{\min})$ the measured upper limit at $E_{\min} \sim 0.1$ MeV, the ratio $F_{UL}(E)/F_{KP}(E)$ may reach ~0.6–0.7 at 0.20–0.28 MeV for $\beta \sim 0.8$ in the case of strong electron injections mainly occurring only up to $E_0 \sim 0.1$ MeV. However, $F_{UL}(E)/F_{KP}(E)$ can remain close to 1 from 0.1 to 0.6 MeV during strong injections extending up to $E_0 \sim 0.2$ MeV. Taking into account measurement uncertainties, distinguishing between these two upper limits may be often impracticable. Nevertheless, the opposite variations of $\partial F_{UL}/\partial E$ and $\partial F_{KP}/\partial E$ as a function of $\Omega_{pe0}/\Omega_{ce0}$ could amplify the differences between these two upper limits during particular events with a high $\Omega_{pe0}/\Omega_{ce0}$ ratio.

5. Comparisons With Measured Trapped and Precipitating Electron Fluxes During Selected Events

The theoretical upper limit $J_{UL}(E) = F_{UL}(E) \cdot c\left(E^2 + E\right)^{1/2}/(E + 1/2)$ on the differential electron flux (with F_{UL} given in Section 4.2) is compared below with trapped electron fluxes $J(E)$ measured near the magnetic equator by the Van Allen Probes (Mauk et al., 2013) at adiabatically invariant shells $L^* \simeq 4.5$–5 (determined using the TS04 magnetic field model, see Tsyganenko & Sitnov, 2005) during the recovery phase of four moderate geomagnetic storms with a minimum $Dst \in [-65, -49]$ nT. Most storms within this minimum Dst range produce a growing peak of ∼1.5 MeV electron PSD centered at $L^* \sim 4.8$, which is a characteristic signature of local chorus wave-driven electron acceleration (Boyd et al., 2018). The moderate minimum Dst should also ensure that the effects of chorus wave-driven energization on electron fluxes prevail over the Dst effect (Kim & Chan, 1997) at $L^* \leq 5$.

We especially selected four events of particularly high time-integrated geomagnetic activity $Int(AE) > 40{,}000$ nT·hr (with AE the auroral electrojet index) or $Int(ap) > 2300$ nT·hr (with ap the middle-latitude range index), because such periods correspond to sustained ∼100–300 keV electron injections and strong chorus wave-driven electron acceleration, which are known to produce the highest time-integrated 2-MeV electron fluxes recorded at $L^* \simeq 4$–5 (Hua, Bortnik, & Ma, 2022; Mourenas, Agapitov, et al., 2022; Mourenas et al., 2019). Empirical plasmapause models (O'Brien & Moldwin, 2003) indicate that the plasmapause was at $L \leq 3.8$ during the four selected periods. Since Van Allen Probes statistics have demonstrated the presence of mainly short chorus wave packets separated by large random phase jumps (Zhang et al., 2018; Zhang et al., 2019; Zhang, Agapitov, et al., 2020; Zhang, Mourenas, et al., 2020), the quasi-linear theory used for deriving the steady-state upper limit $J_{UL}(E)$ is expected to remain approximately applicable in most situations, even for relatively intense waves (Z. An et al., 2022; Artemyev et al., 2022; Gan et al., 2022; Mourenas et al., 2018; Mourenas et al., 2021; Mourenas, Zhang, et al., 2022; Zhang, Agapitov, et al., 2020).

Figure 4 shows the maximum measured trapped electron fluxes $J(E, t)$ (black curves) at $L^\star = 4.5$ or 5, at the end of the four selected events of strong electron injection and acceleration up to 2 MeV in 2016–2019 (i.e., at the time when ∼2 MeV electron flux reached its maximum level). We use level-2 spin-averaged omnidirectional electron fluxes measured by the Magnetic Electron Ion Spectrometer (MagEIS) (Claudepierre et al., 2021) of the Energetic Particle, Composition, and Thermal Plasma (ECT) Suite (Spence et al., 2013) on board the Van Allen Probes. During the three periods examined in Figures 4a–4c, Olifer et al. (2022) have shown that the electron flux roughly reached the Kennel-Petschek flux limit $J_{KP}(E)$ at ∼0.1–0.3 MeV. During the fourth event displayed in Figure 4d, a growing peak of PSD of 2–4 MeV electrons, recorded by the Van Allen Probes at $L^* \simeq 4.5$, was not reproduced by simulations of ULF wave-driven electron inward radial diffusion without chorus-driven acceleration, suggesting a key role of chorus wave-driven energization during this storm (Hudson et al., 2021; Mourenas, Artemyev, et al., 2022).

The maximum trapped electron fluxes $J(E, t)$ measured at the end of these events (black curves) are compared in Figure 4 with the shape of the analytical equilibrium upper limit $J_{UL}(E)$ (solid blue curve), corresponding to $F_{UL}(E) \sim F_{st}(E)$ from Equation 20 with $F_{st}(E)$ from Equation 7 with $b = 0$ and $\epsilon(E)$ from Equation 4, based on chorus wave statistics for average $Kp \geq 4$ and $AE \geq 400$ nT as during these four events. These comparisons demonstrate a good agreement from 0.1 MeV up to 0.6–0.7 MeV during all four events. Discrepancies between the steady-state upper limit $J_{UL}(E)$ and measured trapped fluxes $J(E, t)$ within this energy range (0.1–0.7 MeV) could stem from the continuous presence of time-varying injections and/or from differences between the actual chorus wave power distribution in latitude and MLT during a given event and the assumed statistical time-averaged chorus wave power distribution.

At higher energy $E > 0.7$ MeV, the measured flux $J(E, t)$ is usually lower than the upper limit $J_{UL}(E)$ estimated based on chorus wave-driven energization and loss. This could sometimes be due to an insufficiently long event duration, preventing $J(E, t)$ from increasing up to its upper limit $J_{UL}(E)$ (Hua, Bortnik, & Ma, 2022; Mourenas, Artemyev, et al., 2022). But it can also be due to a faster electron precipitation above ∼1 MeV in the additional presence of EMIC waves inside a noon-duskside plasmaspheric plume (Ross et al., 2021; Zhang et al., 2016), at the same $L^\star$ as contemporaneous chorus waves in the midnight-to-noon sector outside the plasmasphere (Drozdov et al., 2020; Mourenas et al., 2016, 2021; Zhang et al., 2017). In the presence of combined EMIC and chorus wave-driven electron pitch-angle diffusion and chorus wave-driven energy diffusion, the equilibrium steady-state

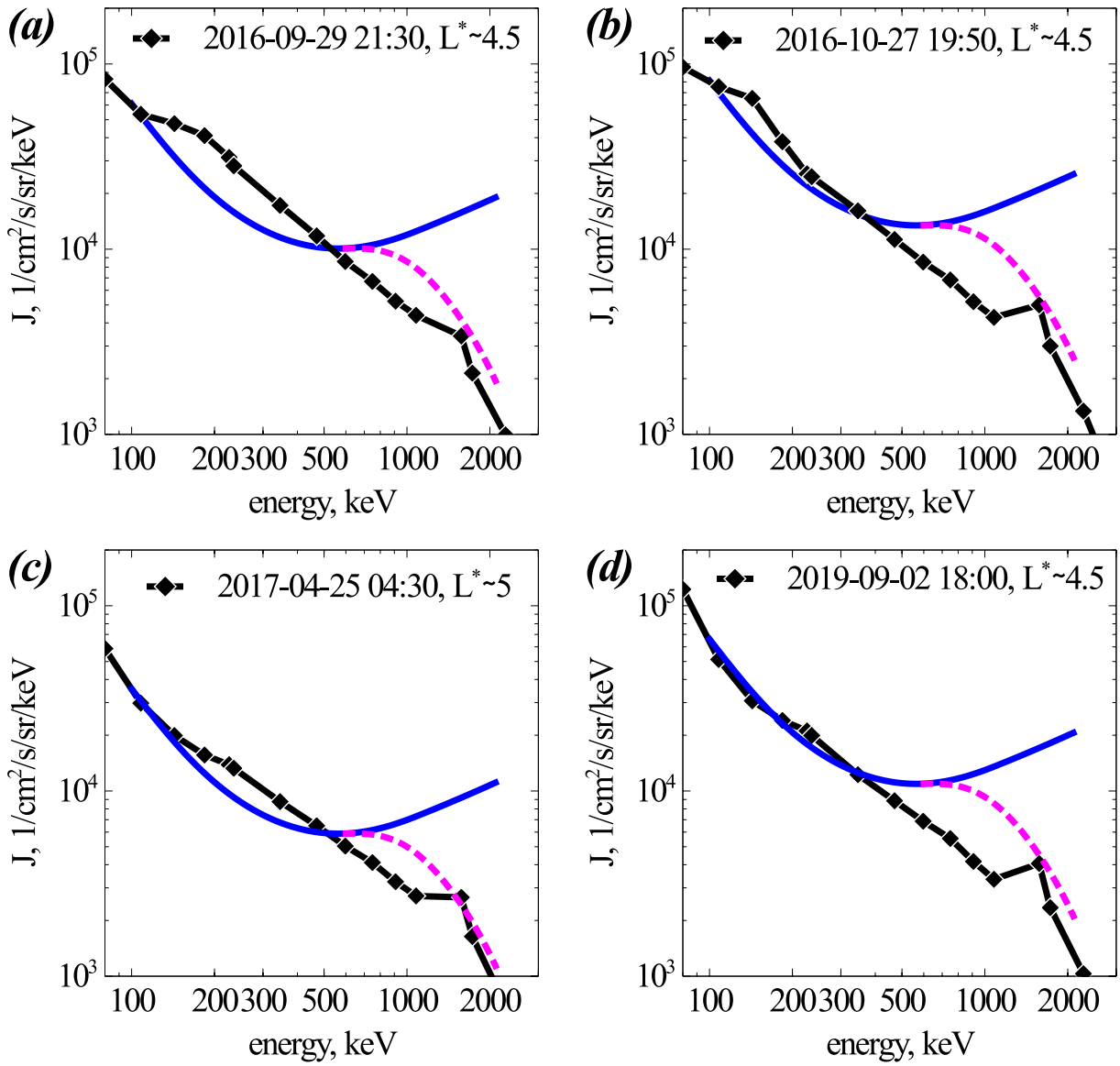

Figure 4. (a) Trapped omnidirectional electron flux $J(E, t)$ measured at $L^\star = 4.5$ near the magnetic equator by the Van Allen Probes on 29 September 2016 (black), at the end of an event of strong electron injection and acceleration up to 2 MeV. The approximate analytical equilibrium upper limit $J_{UL}(E) = F_{UL}(E) \cdot c\left(E^2 + E\right)^{1/2}/(E + 1/2)$, with $F_{UL}(E) \sim F_{st}(E)$ given by Equations 20 and 7 with $b = 0$ and $\epsilon(E)$ from Equation 4, is shown (solid blue) normalized to $J(E_{\min})$ at $E_{\min} = 0.1$ MeV. The approximate, lower steady-state upper limit $J_{ULL}(E)$ given by Equation 24 for $E > 0.6$ MeV in the presence of contemporaneous EMIC and chorus wave-driven electron precipitation, is also shown (dashed purple). (b) Same as (a) for $J(E)$ measured at $L^\star = 4.5$ on 27 October 2016. (c) Same as (a) for $J(E)$ measured at $L^\star = 5$ on 25 April 2017. (d) Same as (a) for $J(E)$ measured at $L^\star = 4.5$ on 2 September 2019.

electron flux should indeed be reduced above ~0.6 MeV, leading to a lower upper limit $J_{ULL}(E)$ approximately given by

$$J_{ULL}(E) \approx J_{UL}(0.6\,\text{MeV}) \cdot \left(\frac{E}{0.6}\right)^{\alpha} \exp(2(0.6 - E)\alpha)\, \frac{1.12\left(E^2 + E\right)^{1/2}}{(E + 1/2)} \tag{24}$$

at $E > 0.6$ MeV, with $\alpha = \max(0.5, \tanh(E^2))$ (Mourenas, Artemyev, et al., 2022). A previous study has shown that this reduced upper limit $J_{ULL}(E)$ agrees well with the normalized maximum electron energy spectrum at $E > 0.6$ MeV measured at the end of prolonged events of extreme time-integrated geomagnetic activity *Int*(*AE*) and *Int*(*ap*) in September and November 2003, lasting 4–9 days (Mourenas, Artemyev, et al., 2022). Figure 4 similarly shows a good agreement between $J_{ULL}(E)$ and the maximum measured electron flux above 0.6 MeV

during the four selected events. The main discrepancy at 0.8–1.2 MeV stems from the normalization of J_{ULL} to the chorus-driven upper limit J_{UL}(0.6 MeV), which is sometimes sensibly higher than the measured flux J(0.6 MeV). The flatter slope of $J_{UL}(E)$ and $J_{ULL}(E)$ at 0.5–0.8 MeV than in observations could be due to a stronger chorus wave power at middle latitudes than assumed in the model. Alternatively, it could be due to a non-negligible pitch-angle diffusion of such electrons by EMIC waves, as suggested by several studies (X. An et al., 2022; Angelopoulos et al., 2023; Capannolo et al., 2019; Denton et al., 2019; Hendry et al., 2017; Zhang, Mourenas, et al., 2021).

Next, the approximate theoretical upper limit $J_{UL}(E)$ is compared with observations of trapped and precipitating electron fluxes from ELFIN CubeSats (Angelopoulos et al., 2020) at low altitude during another event of sustained electron injections on 16–18 April 2021. To estimate the theoretical upper limit $J_{prec,UL}$ on the average precipitating electron flux measured in the loss-cone by ELFIN, based on the theoretical upper limit on the trapped flux J_{UL}, we use the full quasi-linear expressions for the precipitating to trapped flux ratio $J_{prec}(\alpha_0)/J_{trap}(\alpha_{0,trap})$ (Kennel & Petschek, 1966; Li et al., 2013), with $\alpha_{0,LC}$ the loss-cone angle and $\ln(\sin\alpha_{0,trap}/\sin\alpha_{0,LC}) \sim 1/20$ (Mourenas et al., 2021). Averaging $J_{prec}(\alpha_0)$ over the loss-cone as in the latest ELFIN data release gives $J_{prec}/J_{trap} \simeq 1.8\int_0^1 dx I_0(z_0 y)y/(I_0(z_0)+I_1(z_0)z_0/20)$ with $y = 1.1\sin(1.15x)$, $z_0 = 2\alpha_{0,LC}/\sqrt{\tau_B D_{\alpha\alpha}(\alpha_{0,LC})}$, $D_{\alpha\alpha}(\alpha_{0,LC})$ the chorus wave-driven electron pitch-angle diffusion rate at $\alpha_{0,LC}$, and τ_B the electron bounce period (Kennel & Petschek, 1966). For $J_{prec}/J_{trap} \in [0.001, 0.85]$, we get $J_{prec}/J_{trap} \simeq 1.3/\left(z_0 + z_0^2/200\right)$, with less than ~25% error (Mourenas, Zhang, et al., 2022). Over 0.1–0.5 MeV, $D_{\alpha\alpha}$ varies with energy like $B^2_{w.loss}/\left((E+1/2)\left(E^2+E\right)^{7/9}\right)$ in the case of electron diffusion by quasi-parallel lower band chorus waves (Mourenas, Artemyev, Agapitov, & Krasnoselskikh, 2014) prevalent when $Kp \gtrsim 4$ (e.g., see Agapitov et al., 2018).

Assuming that the average chorus wave power $B^2_{w.loss}$ at latitudes of cyclotron resonance with electrons near the loss-cone during disturbed periods with $Kp \sim 4$–5 is similar to its time-averaged level in Van Allen Probes and Cluster spacecraft data at 4–12 MLT (Agapitov et al., 2018), its variation with E is approximately given by the middle term on the right-hand-side of Equation 4. During sustained electron injections, such that the trapped flux J_{trap} reaches its upper limit J_{UL} and $J_{prec}/J_{trap} > 0.1$, this gives a scaling law for the upper limit on the precipitating electron flux at 4–12 MLT:

$$\frac{J_{prec,UL}}{J_{UL}}[E] \approx \frac{J_{prec,UL}}{J_{UL}}[0.1\,\mathrm{MeV}]\cdot\frac{0.1373}{(E^2+E)^{23/36}(E+6E^5)^{1/4}}. \tag{25}$$

For accurate comparisons with theoretical estimates, the precipitating flux measured by ELFIN is corrected for atmospheric backscatter (Selesnick et al., 2004) in the conjugate hemisphere, to obtain the net electron flux J_{prec} directly precipitated by wave-driven diffusion alone (Mourenas et al., 2021). This is achieved approximately, assuming a rough North-South symmetry about the equator over times long compared to a bounce period, by subtracting the measured upward electron flux backscattered in the loss cone by the atmosphere below ELFIN from the downward precipitating flux measured at ELFIN (Mourenas et al., 2021). As in previous work, we use the trapped or quasi-trapped (hereafter simply called trapped) electron flux J_{trap} measured by the sun-synchronous ELFIN A CubeSat at a fixed MLT (6:20 MLT here) and a fixed longitude (away from the South Atlantic Anomaly), where the trapped flux usually varies smoothly during an event (e.g., see Mourenas et al., 2021).

We examine a moderate geomagnetic storm on 16–18 April 2021, reaching a minimum $Dst \simeq -54$ nT at 5 UT on 17 April. During this storm, the average Kp was ~4 from 18 UT on 16 April to 12 UT on 18 April, and Kp reached 4.7–5.0 during the first 15 hr, corresponding to significant injections. Based on empirical plasmapause models (O'Brien & Moldwin, 2003), the plasmasphere was then limited to $L < 4$. The ratio J_{prec}/J_{trap} of net precipitating to trapped electron flux measured at low altitude ~450 km by ELFIN A at $L \sim 4.5$–5.5 (outside the plasmasphere) is displayed in Figure 5a. It shows that $J_{prec}/J_{trap} < 0.3$ above 100 keV during this event, corresponding to a weak diffusion regime (Kennel, 1969; Li et al., 2013; Mourenas et al., 2021). In this regime, one can use $F_{UL}(E) = F_{st}(E,\epsilon)$ given by Equation 7 with $b = 0$ (or by Equations 9 and 11 with $b = 0$), where $\epsilon(E)$ is provided by Equation 4. In the strong diffusion regime, where $J_{prec}/J_{trap} \simeq 1$, one should rather use $F_{UL}(E) = F_{st}(E, \epsilon = 0)$ given by Equations 10 and 11 with $b = 0$ and $\epsilon = 0$.

In Figure 5b, the energy spectrum $J_{trap}(E)$ of the trapped or quasi-trapped electron flux measured by ELFIN A at $\alpha_{0,trap} \simeq 1.05\ \alpha_{0,LC}$ just outside the bounce loss cone is displayed at three different times during this storm. J_{trap} increases at 100–200 keV from 16 to 17–18 April 2021 due to injections. Chorus wave-driven electron

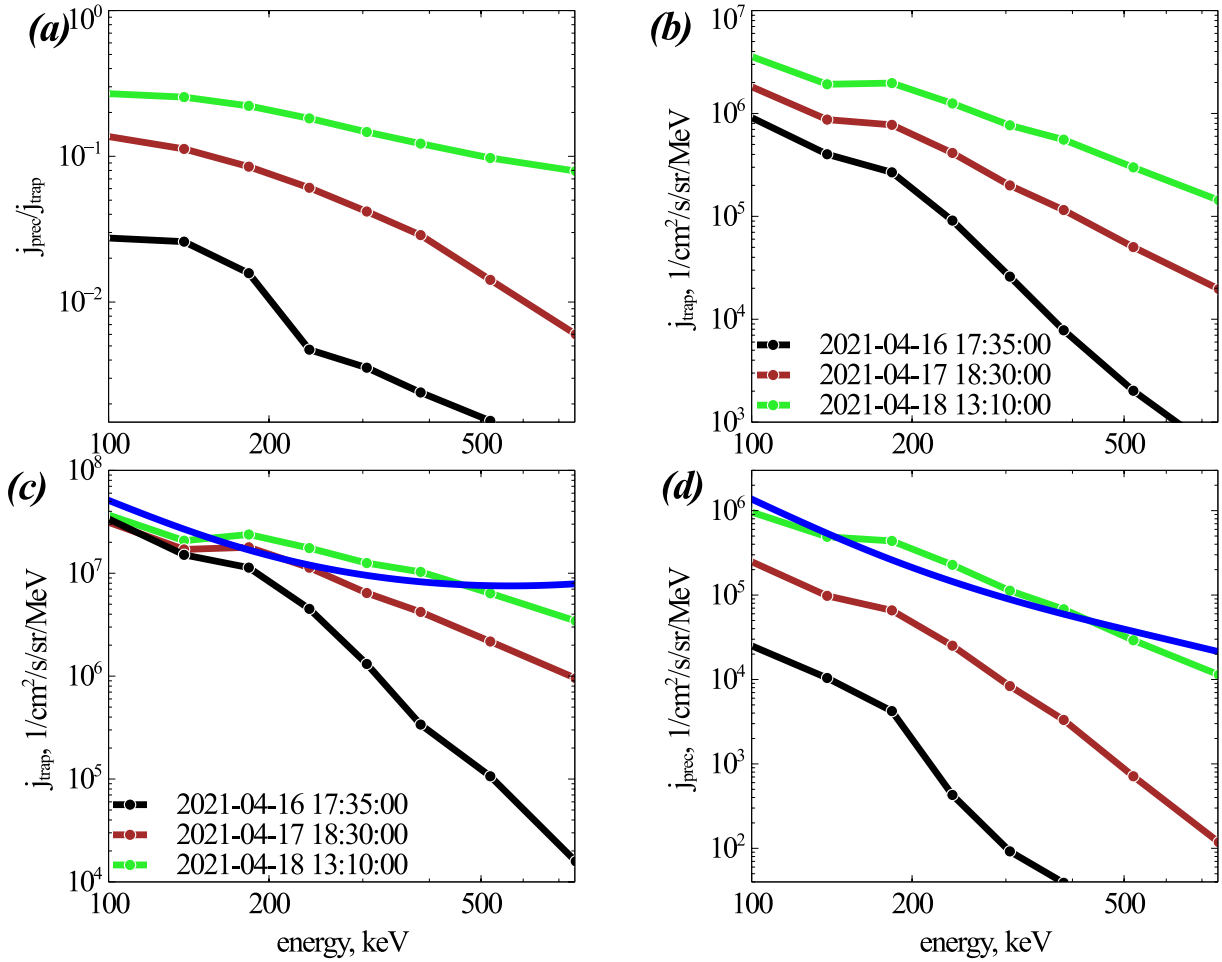

Figure 5. (a) Ratio J_{prec}/J_{trap} of net precipitating to trapped electron flux measured at low altitude by ELFIN A at $L = 4.5$–5.5 near 6:20 MLT, averaged over ∼30 spacecraft spins (i.e., 1.5 min) at 17:35 UT on 16 April 2021 (black), at 18:30 UT on 17 April (brown), and at 13:10 UT on 18 April (green), using data well above instrument noise level (3 counts/s). (b) Trapped electron flux $J_{trap}(\alpha_{0,trap})$ measured by ELFIN A at $L \simeq 5$ just above the loss cone near 6:20 MLT. (c) Trapped electron flux $J_{trap}(\alpha_0 = 90°)$ inferred from $J_{trap}(\alpha_{0,trap})$ and J_{prec}/J_{trap} measured by ELFIN A, using Equation 26 from quasi-linear theory. The theoretical equilibrium upper limit $J_{UL}(E) \sim J_{st}(E)$ (blue) is given by Equations 20 and 7 with $b = 0$ and $\epsilon(E)$ from Equation 4, normalized to minimize the root-mean-square deviation at 100–600 keV on 18 April. (d) Net measured precipitating electron flux J_{prec} (averaged over the loss cone), calculated after subtraction of the measured upward flux backscattered within the loss cone. The upper limit $J_{prec,UL}(E)$ given by Equation 25 based on the same estimate of $J_{st}(E, \epsilon)$ as in (c) is shown (blue), normalized to minimize the root-mean-square deviation on 18 April.

energization simultaneously leads to an even stronger increase of J_{trap} at higher energy ∼400 − 750 keV from a very low initial level (Thorne et al., 2013). The simultaneous presence of intense chorus waves is attested by the increase of J_{prec}/J_{trap} from ∼0.03 on 16 April to ∼0.3 on 18 April in Figure 5a, since J_{prec}/J_{trap} is roughly proportional to the square root of the chorus-driven diffusion rate $D_{\alpha\alpha}(\alpha_{0,LC})$.

Assuming a quasi-equilibrium state, the trapped electron flux at $\alpha_0 = 90°$ can be inferred from the trapped flux measured by ELFIN at $\alpha_{0,trap} \simeq 1.05\ \alpha_{0,LC}$, since quasi-linear diffusion theory (Kennel & Petschek, 1966; Li et al., 2013) gives

$$\frac{J_{trap}(\alpha_0 = 90°)}{J_{trap}(\alpha_{0,trap})} \approx \frac{1 + z_0 \frac{I_1(z_0)}{I_0(z_0)} \ln\left(\frac{1}{\sin\alpha_{0,LC}}\right)}{1 + z_0 \frac{I_1(z_0)}{I_0(z_0)} \ln\left(\frac{\sin\alpha_{0,trap}}{\sin\alpha_{0,LC}}\right)}, \tag{26}$$

with $\alpha_{0,LC} \simeq 3.75°$ at $L \simeq 5$, and where z_0 can be inferred from the precipitating to trapped flux ratio J_{prec}/J_{trap} simultaneously measured by ELFIN (see Figure 5a) via the approximate formula $z_0 \simeq \left(10^4 + 260\, J_{trap}/J_{prec}\right)^{1/2} - 100$, with less than 25% error for $J_{prec}/J_{trap} \in [0.001, 0.85]$ (Mourenas, Zhang, et al., 2022). Although Equation 26

was originally derived assuming a diffusion rate of the form $D_{\alpha\alpha}(\alpha_0) \sim 1/\cos\alpha_0$ (Kennel & Petschek, 1966), we checked that adopting a more realistic form $D_{\alpha\alpha}(\alpha_0) \sim 1/\cos^2\alpha_0$ (Agapitov et al., 2018; Mourenas, Artemyev, Ripoll, et al., 2012) leads to a negligible (<11%) change of $J_{trap}(\alpha_0 = 90°)/J_{trap}(\alpha_{0,trap})$.

At 13:10 UT on 18 April 2021, we get $z_0 = 4.5$ at 100 keV and Equation 26 gives a ratio $J_{trap}(\alpha_0 = 90°)/J_{trap}(\alpha_{0,trap}) \approx 10$, equivalent to a pitch-angle distribution shape $J_{trap}(\alpha_0) = \sin^{2s}\alpha_0$ with $s = 0.3$ at $\alpha_0 > 10°$, while at 750 keV we get $s = 0.32$. Such values of s are typical during strong injections reaching the Kennel-Petschek limit at 100 keV (Olifer et al., 2022). Figure 5c demonstrates that sustained electron injections and chorus wave-driven electron energization and precipitation led the trapped flux $J_{trap}(E)$ to reach on 18 April the same shape as the theoretical equilibrium upper limit $J_{UL}(E) \sim J_{st}(E, \epsilon)$ given by Equations 20 and 7 with $b = 0$ and $\epsilon(E)$ from Equation 4, from 100 to 600 keV (compare green and blue curves). In Figure 5d, the measured net precipitating flux $J_{prec}(E)$ on 18 April is also in good agreement with the theoretical estimate $J_{prec,UL}(E)$ of its upper limit based on Equation 25 up to 600 keV.

For events lasting more than 24 hr in the weak diffusion regime, Equation 19 provides an estimate of the injection strength at 100 keV, $F_S/\tau_S \approx F_{UL}/\tau_L$. The maximum trapped flux J_{trap} at $\alpha_0 = 90°$ on 18 April 2021 at 13:10 UT has been inferred from the maximum trapped flux measured by ELFIN just above the loss cone (see Figure 5c), giving $J_{UL} \approx J_{trap} \approx 3\ 10^7$ e/cm^2/s/sr/MeV at 100 keV. This is close to the maximum trapped flux measured by the Van Allen Probes near the magnetic equator during the April 2017 event in Figure 4c. ELFIN measurements on 16–18 April 2021 in Figure 5a further suggest a time-averaged $J_{prec}/J_{trap} \approx 0.13$ at 100 keV during this event. Based on the above quasi-linear estimates, this corresponds to $D_{\alpha\alpha}(\alpha_{0,LC}) \approx 2 \times 10^{-4}$ s^{-1} at 100 keV and $L \sim 5$ near 6 MLT, in rough agreement with diffusion rates based on the statistical average chorus wave power when $Kp = 4 - 5$ (Agapitov et al., 2018, 2019; Meredith et al., 2020). It corresponds to a 100 keV electron lifetime $\tau_L \approx 5\ 10^3$ s at $L = 5$. Using the above values of J_{UL} and τ_L and integrating over α_0 yields an injection strength of 100 keV electrons $F_S/\tau_S \approx 4$ e/m^3/s/MeV at $L \sim 5$ during the 16–18 April 2021 storm, corresponding to a full replacement of trapped 100 keV electrons over a characteristic time scale $\sim\tau_L \sim 2$ hr.

Observations at $L \simeq 6$–7 show that typical 100 keV electron injections correspond to $J_S \sim 5 \times 10^7$ to 5×10^8 e/cm^2/s/sr/MeV (e.g., Motoba et al., 2020, 2021; Turner et al., 2017), with a typical injection rate $1/\tau_S \sim 1/3$ hr^{-1} (Borovsky & Yakymenko, 2017; Fu et al., 2021; Gabrielse et al., 2014) sometimes reaching $1/\tau_S \sim 1$ hr^{-1} (Keiling et al., 2022). Since $F_S/\tau_S = (1.8/c)J_S/\tau_S$ for ∼100 keV electrons, the typical injection strength at $L \simeq 6$–7 is $F_S/\tau_S \sim 3$ to 30 e/m^3/s/MeV over $\tau_S \sim 3$ hr. Therefore, the injection strength at $L \sim 5$ during the moderate 16–18 April 2021 storm is only slightly lower than typical levels at $L \simeq 6$–7 for a similar injection duration of ∼3 hr. This is consistent with the maximum 100 keV electron fluxes $J_S \sim (3–8) \times 10^7$ e/cm^2/s/sr/MeV measured near $L \sim 5$ during strong injections by the Van Allen Probes (see Figure 4), which are slightly lower than at $L \simeq 6$–7.

6. Conclusions

In this paper, we derived approximate analytical formulas for the upper limit on the trapped electron flux at ∼0.1–1 MeV, corresponding to a dynamical equilibrium between the total electron inflow from injections and the total electron outflow (into the atmosphere) from precipitation, taking into account both chorus wave-driven electron pitch-angle and energy diffusion during disturbed conditions with $Kp \gtrsim 4$ or $AE > 300$ nT in the Earth's outer radiation belt.

We have shown analytically that in the presence of both energy and pitch-angle diffusion, the electron distribution $F(E,t) = J(E,t)(E + 1/2)/c\left(E^2 + E\right)^{1/2}$, with $J(E, t)$ the electron differential flux, should generally tend toward a limiting, asymptotic, steady-state energy spectrum shape $F_{st}(E)$, which represents an attractor for the system dynamics. This steady-state shape corresponds to a balance, at each energy, between electron precipitation loss and the net incoming flow of electrons produced by diffusive energization. Approximate analytical expressions for this steady-state electron energy spectrum $F_{st}(E)$ have been derived, over a much wider parameter domain than in previous works (Mourenas, Artemyev, et al., 2022), in agreement with numerical simulations.

The absolute level of the equilibrium upper limit $F_{UL}(E)$ on this steady-state electron distribution corresponds to a balance between the total number of electrons injected per second and the total number of electrons precipitated per second. Approximate analytical expressions for the corresponding equilibrium upper limit $F_{UL}(E)$ have been obtained, in the weak and strong diffusion regimes, in agreement with numerical simulation both within and above the low-energy injection range.

We have shown that the analytical steady-state energy spectrum of this equilibrium upper limit is in good agreement with maximum trapped electron fluxes measured by the Van Allen Probes near the magnetic equator, or by ELFIN CubeSats at low altitude, during five events of strong and sustained electron injections and chorus wave-driven electron energization in 2016–2021.

The variation of the equilibrium upper limit $F_{UL}(E)$ as a function of energy E is often similar to the variation of the Kennel-Petschek limit $F_{KP}(E)$, which will probably make it difficult to distinguish between these two upper limits based on the measured energy spectrum shape alone, except maybe during events where the ratio $\Omega_{pe0}/\Omega_{ce0}$ is sufficiently high. Alternatively, full numerical simulations precisely incorporating both mechanisms could be used to investigate the parameter domains where each mechanism may be dominant. This is left for future work. Both upper limits should probably be more efficient at ∼0.1–0.6 MeV than at higher energies, due to the only progressive increase of electron flux above 1 MeV through chorus wave-driven energization and due to the additional presence of EMIC wave-driven electron precipitation above 1 MeV.

However, let us caution that the analytical expressions for the equilibrium upper limit on the electron flux derived in the present work are only approximate. In the future, more accurate expressions could easily be obtained from full numerical simulations, including mixed diffusion in addition to energy and pitch-angle diffusion (Albert & Young, 2005). For high wave amplitudes, nonlinear effects should also be carefully examined, both as regards the saturation of the wave amplitude (Mourenas, Zhang, et al., 2022; Omura, 2021) and for the related modifications of quasi-linear pitch-angle and energy diffusion rates (Artemyev et al., 2022).

Data Availability Statement

Van Allen Probes MagEIS electron flux data (REL03 L2) is available at https://rbsp-ect.newmexicoconsortium.org/data_pub/rbspa/mageis. ELFIN data is available at https://data.elfin.ucla.edu/. OMNI data of *AE* and *Kp* are available from the GSFC/SPDF OMNIWeb interface at https://omniweb.gsfc.nasa.gov.

Acknowledgments
A.V.A. and X.-J.Z. acknowledge support by NASA awards 80NSSC23K0403, 80NSSC20K1578 and NSF grants AGS-2019950, and AGS-2329897. V.A. acknowledges ELFIN operations support from NASA NNX14AN68G and ELFIN science support from NSF AGS-1242918.

References

Agapitov, O. V., Mourenas, D., Artemyev, A. V., Hospodarsky, G., & Bonnell, J. W. (2019). Time scales for electron quasi-linear diffusion by lower-band chorus waves: The effects of ω_{pe}/Ω_{ce} dependence on geomagnetic activity. *Geophysical Research Letters*, *46*(12), 6178–6187. https://doi.org/10.1029/2019GL083446

Agapitov, O. V., Mourenas, D., Artemyev, A. V., Mozer, F. S., Hospodarsky, G., Bonnell, J., & Krasnoselskikh, V. (2018). Synthetic empirical chorus wave model from combined Van Allen Probes and cluster statistics. *Journal of Geophysical Research (Space Physics)*, *123*(1), 297–314. https://doi.org/10.1002/2017JA024843

Albert, J. M. (1993). Cyclotron resonance in an inhomogeneous magnetic field. *Physics of Fluids B*, *5*(8), 2744–2750. https://doi.org/10.1063/1.860715

Albert, J. M. (2005). Evaluation of quasi-linear diffusion coefficients for whistler mode waves in a plasma with arbitrary density ratio. *Journal of Geophysical Research*, *110*(A3), 3218. https://doi.org/10.1029/2004JA010844

Albert, J. M. (2009). The coupling of quasi-linear pitch angle and energy diffusion. *Journal of Atmospheric and Solar-Terrestrial Physics*, *71*(16), 1664–1668. https://doi.org/10.1016/j.jastp.2008.11.014

Albert, J. M., & Shprits, Y. Y. (2009). Estimates of lifetimes against pitch angle diffusion. *Journal of Atmospheric and Solar-Terrestrial Physics*, *71*(16), 1647–1652. https://doi.org/10.1016/j.jastp.2008.07.004

Albert, J. M., & Young, S. L. (2005). Multidimensional quasi-linear diffusion of radiation belt electrons. *Geophysical Research Letters*, *32*(14), 14110. https://doi.org/10.1029/2005GL023191

Allanson, O., Watt, C. E. J., Ratcliffe, H., Allison, H. J., Meredith, N. P., Bentley, S. N., et al. (2020). Particle-in-cell experiments examine electron diffusion by whistler-mode waves: 2. Quasi-linear and nonlinear dynamics. *Journal of Geophysical Research (Space Physics)*, *125*(7), e27949. https://doi.org/10.1029/2020JA027949

Allison, H. J., Shprits, Y. Y., Zhelavskaya, I. S., Wang, D., & Smirnov, A. G. (2021). Gyroresonant wave-particle interactions with chorus waves during extreme depletions of plasma density in the Van Allen radiation belts. *Science Advances*, *7*(5), eabc0380. https://doi.org/10.1126/sciadv.abc0380

An, X., Artemyev, A., Angelopoulos, V., Zhang, X., Mourenas, D., & Bortnik, J. (2022a). Nonresonant scattering of relativistic electrons by electromagnetic ion cyclotron waves in Earth's radiation belts. *Physical Review Letters*, *129*(13), 135101. https://doi.org/10.1103/PhysRevLett.129.135101

An, Z., Wu, Y., & Tao, X. (2022b). Electron dynamics in a chorus wave field generated from particle-in-cell simulations. *Geophysical Research Letters*, *49*(3), e2022GL097778. https://doi.org/10.1029/2022GL097778

Angelopoulos, V., Tsai, E., Bingley, L., Shaffer, C., Turner, D. L., Runov, A., et al. (2020). The ELFIN mission. *Space Science Reviews*, *216*(5), 103. https://doi.org/10.1007/s11214-020-00721-7

Angelopoulos, V., Zhang, X.-J., Artemyev, A. V., Mourenas, D., Tsai, E., Wilkins, C., et al. (2023). Energetic electron precipitation driven by electromagnetic ion cyclotron waves from ELFIN's low altitude perspective. *Space Science Reviews*, *219*(37), 37. https://doi.org/10.1007/s11214-023-00984-w

Artemyev, A. V., Mourenas, D., Agapitov, O. V., & Krasnoselskikh, V. V. (2013). Parametric validations of analytical lifetime estimates for radiation belt electron diffusion by whistler waves. *Annales Geophysicae*, *31*(4), 599–624. https://doi.org/10.5194/angeo-31-599-2013

Artemyev, A. V., Mourenas, D., Zhang, X. J., & Vainchtein, D. (2022). On the incorporation of nonlinear resonant wave-particle interactions into radiation belt models. *Journal of Geophysical Research (Space Physics)*, *127*(9), e30853. https://doi.org/10.1029/2022JA030853

Artemyev, A. V., Neishtadt, A. I., Vasiliev, A. A., & Mourenas, D. (2021). Transitional regime of electron resonant interaction with whistler-mode waves in inhomogeneous space plasma. *Physical Review E*, *104*(5), 055203. https://doi.org/10.1103/PhysRevE.104.055203

Aryan, H., Agapitov, O. V., Artemyev, A., Mourenas, D., Balikhin, M. A., Boynton, R., & Bortnik, J. (2020). Outer radiation belt electron lifetime model based on combined Van Allen Probes and cluster VLF measurements. *Journal of Geophysical Research (Space Physics)*, *125*(8), e28018. https://doi.org/10.1029/2020JA028018

Baker, D. N., Stauning, P., Hones, E. W., Jr., Higbie, P. R., & Belian, R. D. (1979). Strong electron pitch angle diffusion observed at geostationary orbit. *Geophysical Research Letters*, *6*(3), 205–208. https://doi.org/10.1029/GL006i003p00205

Bakhareva, M. F. (2003). Nonstationary statistical acceleration of relativistic particles and its role during geomagnetic storms. *Geomagnetism and Aeronomy*, *43*, 687–693.

Bakhareva, M. F. (2005). Time variations in energetic particle fluxes at different types of statistical acceleration and the variation properties during geomagnetic disturbances. *Geomagnetism and Aeronomy*, *45*, 551–561.

Balikhin, M. A., Gedalin, M., Reeves, G. D., Boynton, R. J., & Billings, S. A. (2012). Time scaling of the electron flux increase at GEO: The local energy diffusion model vs observations. *Journal of Geophysical Research*, *117*(A10), 10208. https://doi.org/10.1029/2012JA018114

Borovsky, J. E., & Yakymenko, K. (2017). Substorm occurrence rates, substorm recurrence times, and solar wind structure. *Journal of Geophysical Research (Space Physics)*, *122*(3), 2973–2998. https://doi.org/10.1002/2016JA023625

Boyd, A. J., Spence, H. E., Huang, C.-L., Reeves, G. D., Baker, D. N., Turner, D. L., et al. (2016). Statistical properties of the radiation belt seed population. *Journal of Geophysical Research*, *121*(8), 7636–7646. https://doi.org/10.1002/2016JA022652

Boyd, A. J., Turner, D. L., Reeves, G. D., Spence, H. E., Baker, D. N., & Blake, J. B. (2018). What causes radiation belt enhancements: A survey of the Van Allen Probes era. *Geophysical Research Letters*, *45*(11), 5253–5259. https://doi.org/10.1029/2018GL077699

Camporeale, E., Wilkie, G. J., Drozdov, A. Y., & Bortnik, J. (2022). Data-driven discovery of Fokker-Planck equation for the Earth's radiation belts electrons using physics-informed neural networks. *Journal of Geophysical Research*, *127*(7), e2022JA030377. https://doi.org/10.1029/2022JA030377

Capannolo, L., Li, W., Ma, Q., Shen, X. C., Zhang, X. J., Redmon, R. J., et al. (2019). Energetic electron precipitation: Multievent analysis of its spatial extent during EMIC wave activity. *Journal of Geophysical Research (Space Physics)*, *124*(4), 2466–2483. https://doi.org/10.1029/2018JA026291

Chakraborty, S., Mann, I. R., Watt, C. E. J., Rae, I. J., Olifer, L., Ozeke, L. G., et al. (2022). Intense chorus waves are the cause of flux-limiting in the heart of the outer radiation belt. *Scientific Reports*, *12*(1), 21717. https://doi.org/10.1038/s41598-022-26189-9

Chen, H., Gao, X., Lu, Q., Tsurutani, B. T., & Wang, S. (2020). Statistical evidence for EMIC wave excitation driven by substorm injection and enhanced solar wind pressure in the Earth's magnetosphere: Two different EMIC wave sources. *Geophysical Research Letters*, *47*(21), e2020GL090275. https://doi.org/10.1029/2020GL090275

Chen, L., Thorne, R. M., Li, W., & Bortnik, J. (2013). Modeling the wave normal distribution of chorus waves. *Journal of Geophysical Research*, *118*(3), 1074–1088. https://doi.org/10.1029/2012JA018343

Chen, Y., Reeves, G. D., & Friedel, R. H. W. (2007). The energization of relativistic electrons in the outer Van Allen radiation belt. *Nature Physics*, *3*(9), 614–617. https://doi.org/10.1038/nphys655

Chu, X., Ma, D., Bortnik, J., Tobiska, W. K., Cruz, A., Bouwer, S. D., et al. (2021). Relativistic electron model in the outer radiation belt using a neural network approach. *Space Weather*, *19*(12), e2021SW002808. https://doi.org/10.1029/2021SW002808

Claudepierre, S. G., Blake, J. B., Boyd, A. J., Clemmons, J. H., Fennell, J. F., Gabrielse, C., et al. (2021). The magnetic electron ion spectrometer: A review of on-orbit sensor performance, data, operations, and science. *Space Science Reviews*, *217*(8), 80. https://doi.org/10.1007/s11214-021-00855-2

Daglis, I. A., Katsavrias, C., & Georgiou, M. (2019). From solar sneezing to killer electrons: Outer radiation belt response to solar eruptions. *Philosophical Transactions of the Royal Society A*, *377*(2148), 20180097. https://doi.org/10.1098/rsta.2018.0097

Demekhov, A. G., & Trakhtengerts, V. Y. (2008). Dynamics of the magnetospheric cyclotron ELF/VLF maser in the backward-wave-oscillator regime. II. The influence of the magnetic-field inhomogeneity. *Radiophysics and Quantum Electronics*, *51*(11), 880–889. https://doi.org/10.1007/s11141-009-9093-3

Denton, R. E., Ofman, L., Shprits, Y. Y., Bortnik, J., Millan, R. M., Rodger, C. J., et al. (2019). Pitch angle scattering of sub-MeV relativistic electrons by electromagnetic ion cyclotron waves. *Journal of Geophysical Research (Space Physics)*, *124*(7), 5610–5626. https://doi.org/10.1029/2018JA026384

Denton, R. E., Takahashi, K., Galkin, I. A., Nsumei, P. A., Huang, X., Reinisch, B. W., et al. (2006). Distribution of density along magnetospheric field lines. *Journal of Geophysical Research*, *111*(A4), 4213. https://doi.org/10.1029/2005JA011414

Drozdov, A. Y., Shprits, Y. Y., Orlova, K. G., Kellerman, A. C., Subbotin, D. A., Baker, D. N., et al. (2015). Energetic, relativistic, and ultrarelativistic electrons: Comparison of long-term VERB code simulations with Van Allen Probes measurements. *Journal of Geophysical Research*, *120*(5), 3574–3587. https://doi.org/10.1002/2014JA020637

Drozdov, A. Y., Usanova, M. E., Hudson, M. K., Allison, H. J., & Shprits, Y. Y. (2020). The role of hiss, chorus, and EMIC waves in the modeling of the dynamics of the multi-MeV radiation belt electrons. *Journal of Geophysical Research*, *125*(9), e2020JA028282. https://doi.org/10.1029/2020JA028282

Elliott, S. S., Breneman, A. W., Colpitts, C., Pettit, J. M., Cattell, C. A., Halford, A. J., et al. (2022). Quantifying the size and duration of a microburst-producing chorus region on 5 December 2017. *Geophysical Research Letters*, *49*(15), e2022GL099655. https://doi.org/10.1029/2022GL099655

Etcheto, J., Gendrin, R., Solomon, J., & Roux, A. (1973). A self-consistent theory of plasmaspheric hiss. *Journal of Geophysical Research*, *78*(34), 8150–8166. https://doi.org/10.1029/JA078i034p08150

Fu, H., Yue, C., Zong, Q.-G., Zhou, X.-Z., & Fu, S. (2021). Statistical characteristics of substorms with different intensity. *Journal of Geophysical Research (Space Physics)*, *126*(8), e29318. https://doi.org/10.1029/2021JA029318

Gabrielse, C., Angelopoulos, V., Runov, A., & Turner, D. L. (2014). Statistical characteristics of particle injections throughout the equatorial magnetotail. *Journal of Geophysical Research*, *119*(4), 2512–2535. https://doi.org/10.1002/2013JA019638

Gan, L., Li, W., Ma, Q., Artemyev, A. V., & Albert, J. M. (2022). Dependence of nonlinear effects on whistler-mode wave bandwidth and amplitude: A perspective from diffusion coefficients. *Journal of Geophysical Research*, *127*(5), e2021JA030063. https://doi.org/10.1029/2021JA030063

Glauert, S. A., & Horne, R. B. (2005). Calculation of pitch angle and energy diffusion coefficients with the PADIE code. *Journal of Geophysical Research*, *110*(A4), 4206. https://doi.org/10.1029/2004JA010851

Green, J. C., & Kivelson, M. G. (2004). Relativistic electrons in the outer radiation belt: Differentiating between acceleration mechanisms. *Journal of Geophysical Research*, *109*(A3), A03213. https://doi.org/10.1029/2003JA010153

Hendry, A. T., Rodger, C. J., & Clilverd, M. A. (2017). Evidence of sub-MeV EMIC-driven electron precipitation. *Geophysical Research Letters*, *44*(3), 1210–1218. https://doi.org/10.1002/2016GL071807

Horne, R. B., Thorne, R. M., Glauert, S. A., Albert, J. M., Meredith, N. P., & Anderson, R. R. (2005). Timescale for radiation belt electron acceleration by whistler mode chorus waves. *Journal of Geophysical Research*, *110*, 3225. https://doi.org/10.1029/2004JA010811

Hua, M., Bortnik, J., Chu, X., Aryan, H., & Ma, Q. (2022). Unraveling the critical geomagnetic conditions controlling the upper limit of electron fluxes in the Earth's outer radiation belt. *Geophysical Research Letters*, *49*(22), e2022GL101096. https://doi.org/10.1029/2022GL101096

Hua, M., Bortnik, J., & Ma, Q. (2022). Upper limit of outer radiation belt electron acceleration driven by whistler-mode chorus waves. *Geophysical Research Letters*, *49*(15), e2022GL099618. https://doi.org/10.1029/2022GL099618

Hudson, M. K., Elkington, S. R., Li, Z., Patel, M., Pham, K., Sorathia, K., et al. (2021). MHD-test particles simulations of moderate CME and CIR-driven geomagnetic storms at solar minimum. *Space Weather*, *19*(12), e2021SW002882. https://doi.org/10.1029/2021SW002882

Karpman, V. I., Istomin, J. N., & Shklyar, D. R. (1974). Nonlinear theory of a quasi-monochromatic whistler mode packet in inhomogeneous plasma. *Plasma Physics*, *16*(8), 685–703. https://doi.org/10.1088/0032-1028/16/8/001

Katoh, Y., & Omura, Y. (2007). Relativistic particle acceleration in the process of whistler-mode chorus wave generation. *Geophysical Research Letters*, *34*(13), L13102. https://doi.org/10.1029/2007GL029758

Katoh, Y., Omura, Y., Miyake, Y., Usui, H., & Nakashima, H. (2018). Dependence of generation of whistler mode chorus emissions on the temperature anisotropy and density of energetic electrons in the Earth's inner magnetosphere. *Journal of Geophysical Research*, *123*(2), 1165–1177. https://doi.org/10.1002/2017JA024801

Keiling, A., Ramos, C., Vu, N., Angelopoulos, V., & Nosé, M. (2022). Statistical properties and proposed source mechanism of recurrent substorm activity with one-hour periodicity. *Journal of Geophysical Research (Space Physics)*, *127*(3), e30064. https://doi.org/10.1029/2021JA030064

Kennel, C. F. (1969). Consequences of a magnetospheric plasma. *Reviews of Geophysics and Space Physics*, *7*(1-2), 379–419. https://doi.org/10.1029/RG007i001p00379

Kennel, C. F., & Petschek, H. E. (1966). Limit on stably trapped particle fluxes. *Journal of Geophysical Research*, *71*, 1–28. https://doi.org/10.1029/jz071i001p00001

Kim, H.-J., & Chan, A. A. (1997). Fully adiabatic changes in storm time relativistic electron fluxes. *Journal of Geophysical Research*, *102*(A10), 22107–22116. https://doi.org/10.1029/97JA01814

Li, W., & Hudson, M. K. (2019). Earth's Van Allen radiation belts: From discovery to the Van Allen Probes era. *Journal of Geophysical Research (Space Physics)*, *124*(11), 8319–8351. https://doi.org/10.1029/2018JA025940

Li, W., Ni, B., Thorne, R. M., Bortnik, J., Green, J. C., Kletzing, C. A., et al. (2013). Constructing the global distribution of chorus wave intensity using measurements of electrons by the POES satellites and waves by the Van Allen Probes. *Geophysical Research Letters*, *40*(17), 4526–4532. https://doi.org/10.1002/grl.50920

Li, W., Santolik, O., Bortnik, J., Thorne, R. M., Kletzing, C. A., Kurth, W. S., & Hospodarsky, G. B. (2016). New chorus wave properties near the equator from Van Allen Probes wave observations. *Geophysical Research Letters*, *43*(10), 4725–4735. https://doi.org/10.1002/2016GL068780

Li, W., Shprits, Y. Y., & Thorne, R. M. (2007). Dynamic evolution of energetic outer zone electrons due to wave-particle interactions during storms. *Journal of Geophysical Research*, *112*(A10), 10220. https://doi.org/10.1029/2007JA012368

Lichtenberg, A. J., & Lieberman, M. A. (1983). Regular and stochastic motion.

Lyons, L. R. (1974). Pitch angle and energy diffusion coefficients from resonant interactions with ion-cyclotron and whistler waves. *Journal of Plasma Physics*, *12*(3), 417–432. https://doi.org/10.1017/S002237780002537X

Ma, D., Chu, X., Bortnik, J., Claudepierre, S. G., Tobiska, W. K., Cruz, A., et al. (2022). Modeling the dynamic variability of sub-relativistic outer radiation belt electron fluxes using machine learning. *Space Weather*, *20*(8), e2022SW003079. https://doi.org/10.1029/2022SW003079

Marshall, R. A., & Bortnik, J. (2018). Pitch angle dependence of energetic electron precipitation: Energy deposition, backscatter, and the bounce loss cone. *Journal of Geophysical Research*, *123*, 2412–2423. https://doi.org/10.1002/2017JA024873

Mauk, B. H., & Fox, N. J. (2010). Electron radiation belts of the solar system. *Journal of Geophysical Research*, *115*(A12), 12220. https://doi.org/10.1029/2010JA015660

Mauk, B. H., Fox, N. J., Kanekal, S. G., Kessel, R. L., Sibeck, D. G., & Ukhorskiy, A. (2013). Science objectives and rationale for the radiation belt storm probes mission. *Space Science Reviews*, *179*(1–4), 3–27. https://doi.org/10.1007/s11214-012-9908-y

Meredith, N. P., Horne, R. B., Shen, X.-C., Li, W., & Bortnik, J. (2020). Global model of whistler mode chorus in the near-equatorial region ($|\lambda_m| < 18°$). *Geophysical Research Letters*, *47*(11), e2020GL087311. https://doi.org/10.1029/2020GL087311

Motoba, T., Ohtani, S., Gkioulidou, M., Mitchell, D. G., Ukhorskiy, A. Y., Takahashi, K., et al. (2020). Pitch angle dependence of electron and ion flux changes during local magnetic dipolarization inside geosynchronous orbit. *Journal of Geophysical Research (Space Physics)*, *125*(2), e27543. https://doi.org/10.1029/2019JA027543

Motoba, T., Ohtani, S., Gkioulidou, M., Ukhorskiy, A. Y., Lanzerotti, L. J., & Claudepierre, S. G. (2021). Superposed epoch analysis of dispersionless particle injections inside geosynchronous orbit. *Journal of Geophysical Research (Space Physics)*, *126*(8), e29546. https://doi.org/10.1029/2021JA029546

Mourenas, D., Agapitov, O. V., Artemyev, A. V., & Zhang, X.-J. (2022). A climatology of long-duration high 2-MeV electron flux periods in the outer radiation belt. *Journal of Geophysical Research: Space Physics*, *127*(8), e2022JA030661. https://doi.org/10.1029/2022JA030661

Mourenas, D., Artemyev, A., Agapitov, O., & Krasnoselskikh, V. (2012). Acceleration of radiation belts electrons by oblique chorus waves. *Journal of Geophysical Research*, *117*(A10), 10212. https://doi.org/10.1029/2012JA018041

Mourenas, D., Artemyev, A. V., Agapitov, O. V., & Krasnoselskikh, V. (2014). Consequences of geomagnetic activity on energization and loss of radiation belt electrons by oblique chorus waves. *Journal of Geophysical Research*, *119*(4), 2775–2796. https://doi.org/10.1002/2013JA019674

Mourenas, D., Artemyev, A. V., Agapitov, O. V., Krasnoselskikh, V., & Li, W. (2014). Approximate analytical solutions for the trapped electron distribution due to quasi-linear diffusion by whistler mode waves. *Journal of Geophysical Research*, *119*(12), 9962–9977. https://doi.org/10.1002/2014JA020443

Mourenas, D., Artemyev, A. V., Ma, Q., Agapitov, O. V., & Li, W. (2016). Fast dropouts of multi-MeV electrons due to combined effects of EMIC and whistler mode waves. *Geophysical Research Letters*, *43*(9), 4155–4163. https://doi.org/10.1002/2016GL068921

Mourenas, D., Artemyev, A. V., Ripoll, J.-F., Agapitov, O. V., & Krasnoselskikh, V. V. (2012). Timescales for electron quasi-linear diffusion by parallel and oblique lower-band Chorus waves. *Journal of Geophysical Research*, *117*(A6), A06234. https://doi.org/10.1029/2012JA017717

Mourenas, D., Artemyev, A. V., & Zhang, X.-J. (2019). Impact of significant time-integrated geomagnetic activity on 2-MeV electron flux. *Journal of Geophysical Research: Space Physics*, *124*(6), 4445–4461. https://doi.org/10.1029/2019JA026659

Mourenas, D., Artemyev, A. V., Zhang, X.-J., & Angelopoulos, V. (2022). Extreme energy spectra of relativistic electron flux in the outer radiation belt. *Journal of Geophysical Research: Space Physics*, *127*(11), e2022JA031038. https://doi.org/10.1029/2022JA031038

Mourenas, D., Artemyev, A. V., Zhang, X.-J., Angelopoulos, V., Tsai, E., & Wilkins, C. (2021). Electron lifetimes and diffusion rates inferred from ELFIN measurements at low altitude: First results. *Journal of Geophysical Research: Space Physics*, *126*(11), e2021JA029757. https://doi.org/10.1029/2021JA029757

Mourenas, D., Zhang, X.-J., Artemyev, A. V., Angelopoulos, V., Thorne, R. M., Bortnik, J., & Vasiliev, A. A. (2018). Electron nonlinear resonant interaction with short and intense parallel chorus wave packets. *Journal of Geophysical Research*, *123*(6), 4979–4999. https://doi.org/10.1029/2018JA025417

Mourenas, D., Zhang, X. J., Nunn, D., Artemyev, A. V., Angelopoulos, V., Tsai, E., & Wilkins, C. (2022). Short chorus wave packets: Generation within chorus elements, statistics, and consequences on energetic electron precipitation. *Journal of Geophysical Research (Space Physics)*, *127*(5), e30310. https://doi.org/10.1029/2022JA030310

Murphy, K. R., Watt, C. E. J., Mann, I. R., Rae, I. J., Sibeck, D. G., Boyd, A. J., et al. (2018). The global statistical response of the outer radiation belt during geomagnetic storms. *Geophysical Research Letters*, *45*(9), 3783–3792. https://doi.org/10.1002/2017GL076674

Ni, B., Bortnik, J., Nishimura, Y., Thorne, R. M., Li, W., Angelopoulos, V., & Weatherwax, A. T. (2014). Chorus wave scattering responsible for the Earth's dayside diffuse auroral precipitation: A detailed case study. *Journal of Geophysical Research*, *119*(2), 897–908. https://doi.org/10.1002/2013JA019507

Nogi, T., & Omura, Y. (2023). Upstream shift of generation region of whistler-mode rising-tone emissions in the magnetosphere. *Journal of Geophysical Research*, *128*(3), e2022JA031024. https://doi.org/10.1029/2022JA031024

Nunn, D. (1974). A self-consistent theory of triggered VLF emissions. *Planetary and Space Science*, *22*(3), 349–378. https://doi.org/10.1016/0032-0633(74)90070-1

Nunn, D., Zhang, X. J., Mourenas, D., & Artemyev, A. V. (2021). Generation of realistic short chorus wave packets. *Geophysical Research Letters*, *48*(7), e92178. https://doi.org/10.1029/2020GL092178

O'Brien, T. P., & Moldwin, M. B. (2003). Empirical plasmapause models from magnetic indices. *Geophysical Research Letters*, *30*(4), 1152. https://doi.org/10.1029/2002GL016007

Olifer, L., Mann, I. R., Claudepierre, S. G., Baker, D. N., Spence, H. E., & Ozeke, L. G. (2022). A natural limit to the spectral hardness of worst case electron radiation in the terrestrial Van Allen Belt. *Journal of Geophysical Research*, *127*(8), e2022JA030506. https://doi.org/10.1029/2022JA030506

Olifer, L., Mann, I. R., Kale, A., Mauk, B. H., Claudepierre, S. G., Baker, D. N., & Ozeke, L. G. (2021). A tale of two radiation belts: The energy-dependence of self-limiting electron space radiation. *Geophysical Research Letters*, *48*(20), e2021GL095779. https://doi.org/10.1029/2021GL095779

Omura, Y. (2021). Nonlinear wave growth theory of whistler-mode chorus and hiss emissions in the magnetosphere. *Earth Planets and Space*, *73*(1), 95. https://doi.org/10.1186/s40623-021-01380-w

Omura, Y., Hikishima, M., Katoh, Y., Summers, D., & Yagitani, S. (2009). Nonlinear mechanisms of lower-band and upper-band VLF chorus emissions in the magnetosphere. *Journal of Geophysical Research*, *114*(A7), 7217. https://doi.org/10.1029/2009JA014206

Omura, Y., Katoh, Y., & Summers, D. (2008). Theory and simulation of the generation of whistler-mode chorus. *Journal of Geophysical Research*, *113*(A4), 4223. https://doi.org/10.1029/2007JA012622

Omura, Y., & Nunn, D. (2011). Triggering process of whistler mode chorus emissions in the magnetosphere. *Journal of Geophysical Research*, *116*(A5), A05205. https://doi.org/10.1029/2010JA016280

Omura, Y., Nunn, D., & Summers, D. (2013). Generation processes of whistler mode chorus emissions: Current status of nonlinear wave growth theory. In D. Summers, I. U. Mann, D. N. Baker, & M. Schulz (Eds.), *Dynamics of the Earth's radiation belts and inner magnetosphere* (pp. 243–254). https://doi.org/10.1029/2012GM001347

Ross, J. P. J., Glauert, S. A., Horne, R. B., Watt, C. E. J., & Meredith, N. P. (2021). On the variability of EMIC waves and the consequences for the relativistic electron radiation belt population. *Journal of Geophysical Research: Space Physics*, *126*(12), e2975426. https://doi.org/10.1029/2021JA029754

Runov, A., Angelopoulos, V., Gabrielse, C., Liu, J., Turner, D. L., & Zhou, X.-Z. (2015). Average thermodynamic and spectral properties of plasma in and around dipolarizing flux bundles. *Journal of Geophysical Research*, *120*(6), 4369–4383. https://doi.org/10.1002/2015JA021166

Schulz, M. (1974a). Particle lifetimes in strong diffusion. *Astrophysics and Space Science*, *31*(1), 37–42. https://doi.org/10.1007/BF00642599

Schulz, M. (1974b). Particle saturation of the outer zone: A nonlinear model. *Astrophysics and Space Science*, *29*(1), 233–242. https://doi.org/10.1007/BF00642726

Schulz, M., & Davidson, G. T. (1988). Limiting energy spectrum of a saturated radiation belt. *Journal of Geophysical Research*, *93*(A1), 59–76. https://doi.org/10.1029/JA093iA01p00059

Schulz, M., & Lanzerotti, L. J. (1974). *Particle diffusion in the radiation belts*. Springer.

Selesnick, R. S., Looper, M. D., & Albert, J. M. (2004). Low-altitude distribution of radiation belt electrons. *Journal of Geophysical Research*, *109*(A11), A11209. https://doi.org/10.1029/2004JA010611

Shapiro, V. D., & Sagdeev, R. Z. (1997). Nonlinear wave-particle interaction and conditions for the applicability of quasilinear theory. *Physics Reports*, *283*(1–4), 49–71. https://doi.org/10.1016/S0370-1573(96)00053-1

Sheeley, B. W., Moldwin, M. B., Rassoul, H. K., & Anderson, R. R. (2001). An empirical plasmasphere and trough density model: CRRES observations. *Journal of Geophysical Research*, *106*(A11), 25631–25642. https://doi.org/10.1029/2000JA000286

Shklyar, D. R. (1981). Stochastic motion of relativistic particles in the field of a monochromatic wave. *Soviet Physics Journal of Experimental and Theoretical Physics*, *53*, 1197–1192.

Shklyar, D. R., & Matsumoto, H. (2009). Oblique whistler-mode waves in the inhomogeneous magnetospheric plasma: Resonant interactions with energetic charged particles. *Surveys in Geophysics*, *30*(2), 55–104. https://doi.org/10.1007/s10712-009-9061-7

Simms, L. E., Ganushkina, N. Y., Van der Kamp, M., Balikhin, M., & Liemohn, M. W. (2023). Predicting geostationary 40–150 keV electron flux using ARMAX (an autoregressive moving average transfer function), RNN (a recurrent neural network), and logistic regression: A comparison of models. *Space Weather*, *21*, e2022SW003263. https://doi.org/10.1029/2022SW003263

Spence, H. E., Reeves, G. D., Baker, D. N., Blake, J. B., Bolton, M., Bourdarie, S., et al. (2013). Science goals and overview of the radiation belt storm probes (RBSP) energetic particle, composition, and thermal plasma (ECT) suite on NASA's Van Allen Probes mission. *Space Science Reviews*, *179*(1–4), 311–336. https://doi.org/10.1007/s11214-013-0007-5

Su, Z., Zhu, H., Xiao, F., Zheng, H., Wang, Y., Zong, Q.-G., et al. (2014). Quantifying the relative contributions of substorm injections and chorus waves to the rapid outward extension of electron radiation belt. *Journal of Geophysical Research*, *119*(12), 10023–10040. https://doi.org/10.1002/2014JA020709

Summers, D., Ma, C., Meredith, N. P., Horne, R. B., Thorne, R. M., Heynderickx, D., & Anderson, R. R. (2002). Model of the energization of outer-zone electrons by whistler-mode chorus during the October 9, 1990 geomagnetic storm. *Geophysical Research Letters*, *29*(24), 27-1–27-4. https://doi.org/10.1029/2002GL016039

Summers, D., & Ma, C.-Y. (2000). A model for generating relativistic electrons in the Earth's inner magnetosphere based on gyroresonant wave-particle interactions. *Journal of Geophysical Research*, *105*(A2), 2625–2640. https://doi.org/10.1029/1999JA900444

Summers, D., & Shi, R. (2014). Limiting energy spectrum of an electron radiation belt. *Journal of Geophysical Research*, *119*(8), 6313–6326. https://doi.org/10.1002/2014JA020250

Summers, D., & Stone, S. (2022). Analysis of radiation belt killer electron energy spectra. *Journal of Geophysical Research*, *127*(9), e2022JA030698. https://doi.org/10.1029/2022JA030698

Summers, D., Tang, R., & Omura, Y. (2011). Effects of nonlinear wave growth on extreme radiation belt electron fluxes. *Journal of Geophysical Research*, *116*(A10), 10226. https://doi.org/10.1029/2011JA016602

Summers, D., Tang, R., & Thorne, R. M. (2009). Limit on stably trapped particle fluxes in planetary magnetospheres. *Journal of Geophysical Research*, *114*(A10), 10210. https://doi.org/10.1029/2009JA014428

Summers, D., Thorne, R. M., & Xiao, F. (1998). Relativistic theory of wave-particle resonant diffusion with application to electron acceleration in the magnetosphere. *Journal of Geophysical Research*, *103*(A9), 20487–20500. https://doi.org/10.1029/98JA01740

Tang, C., Yang, C., Chen, J., Wang, X., Ni, B., Su, Z., & Zhang, J. (2023). Rapid enhancements of relativistic electrons in the Earth's outer radiation belt caused by the intense substorms: A statistical study. *Journal of Geophysical Research*, *128*(2), e2022JA031089. https://doi.org/10.1029/2022JA031089

Tang, C. L., Wang, Y. X., Ni, B., Su, Z. P., Reeves, G. D., Zhang, J.-C., et al. (2017). The effects of magnetospheric processes on relativistic electron dynamics in the Earth's outer radiation belt. *Journal of Geophysical Research*, *122*(10), 9952–9968. https://doi.org/10.1002/2017JA024407

Tao, X., Bortnik, J., Albert, J. M., Liu, K., & Thorne, R. M. (2011). Comparison of quasilinear diffusion coefficients for parallel propagating whistler mode waves with test particle simulations. *Geophysical Research Letters*, *38*(6), 6105. https://doi.org/10.1029/2011GL046787

Tao, X., Bortnik, J., Albert, J. M., Thorne, R. M., & Li, W. (2013). The importance of amplitude modulation in nonlinear interactions between electrons and large amplitude whistler waves. *Journal of Atmospheric and Solar-Terrestrial Physics*, *99*, 67–72. https://doi.org/10.1016/j.jastp.2012.05.012

Tao, X., Zonca, F., & Chen, L. (2021). A "trap-release-amplify" model of chorus waves. *Journal of Geophysical Research: Space Physics*, *126*(9), e2021JA029585. https://doi.org/10.1029/2021JA029585

Tao, X., Zonca, F., Chen, L., & Wu, Y. (2020). Theoretical and numerical studies of chorus waves: A review. *Science China Earth Sciences*, *63*(1), 78–92. https://doi.org/10.1007/s11430-019-9384-6

Thorne, R. M., Li, W., Ni, B., Ma, Q., Bortnik, J., Chen, L., et al. (2013). Rapid local acceleration of relativistic radiation-belt electrons by magnetospheric chorus. *Nature*, *504*(7480), 411–414. https://doi.org/10.1038/nature12889

Tsurutani, B. T., Lakhina, G. S., & Hajra, R. (2020). The physics of space weather/solar-terrestrial physics (STP): What we know now and what the current and future challenges are. *Nonlinear Processes in Geophysics*, *27*(1), 75–119. https://doi.org/10.5194/npg-27-75-2020

Tsyganenko, N. A., & Sitnov, M. I. (2005). Modeling the dynamics of the inner magnetosphere during strong geomagnetic storms. *Journal of Geophysical Research*, *110*(A3), A03208. https://doi.org/10.1029/2004JA010798

Turner, D. L., Angelopoulos, V., Li, W., Hartinger, M. D., Usanova, M., Mann, I. R., & Shprits, Y. (2013). On the storm-time evolution of relativistic electron phase space density in Earth's outer radiation belt. *Journal of Geophysical Research*, *118*(5), 2196–2212. https://doi.org/10.1002/jgra.50151

Turner, D. L., Claudepierre, S. G., Fennell, J. F., O'Brien, T. P., Blake, J. B., Lemon, C., et al. (2015). Energetic electron injections deep into the inner magnetosphere associated with substorm activity. *Geophysical Research Letters*, *42*(7), 2079–2087. https://doi.org/10.1002/2015GL063225

Turner, D. L., Fennell, J. F., Blake, J. B., Claudepierre, S. G., Clemmons, J. H., Jaynes, A. N., et al. (2017). Multipoint observations of energetic particle injections and substorm activity during a conjunction between magnetospheric multiscale (MMS) and Van Allen Probes. *Journal of Geophysical Research (Space Physics)*, *122*(11), 11481–11504. https://doi.org/10.1002/2017JA024554

Vainchtein, D., Zhang, X. J., Artemyev, A. V., Mourenas, D., Angelopoulos, V., & Thorne, R. M. (2018). Evolution of electron distribution driven by nonlinear resonances with intense field-aligned chorus waves. *Journal of Geophysical Research (Space Physics)*, *123*(10), 8149–8169. https://doi.org/10.1029/2018JA025654

Yang, C., Su, Z., Xiao, F., Zheng, H., Wang, Y., Wang, S., et al. (2016). Rapid flattening of butterfly pitch angle distributions of radiation belt electrons by whistler-mode chorus. *Geophysical Research Letters*, *43*(16), 8339–8347. https://doi.org/10.1002/2016GL070194

Zhang, K., Li, X., Zhao, H., Xiang, Z., Khoo, L. Y., Zhang, W., & Temerin, M. A. (2021). Upper limit of electron fluxes observed in the radiation belts. *Journal of Geophysical Research*, *126*(1), e2020JA028511. https://doi.org/10.1029/2020JA028511

Zhang, X. J., Agapitov, O., Artemyev, A. V., Mourenas, D., Angelopoulos, V., Kurth, W. S., & Hospodarsky, G. B. (2020). Phase decoherence within intense chorus wave packets constrains the efficiency of nonlinear resonant electron acceleration. *Geophysical Research Letters*, *47*(20), e89807. https://doi.org/10.1029/2020GL089807

Zhang, X.-J., Angelopoulos, V., Mourenas, D., Artemyev, A., Tsai, E., & Wilkins, C. (2022). Characteristics of electron microburst precipitation based on high-resolution ELFIN measurements. *Journal of Geophysical Research (Space Physics)*, *127*(5), e30509. https://doi.org/10.1029/2022JA030509

Zhang, X. J., Demekhov, A. G., Katoh, Y., Nunn, D., Tao, X., Mourenas, D., et al. (2021). Fine structure of chorus wave packets: Comparison between observations and wave generation models. *Journal of Geophysical Research (Space Physics)*, *126*(8), e29330. https://doi.org/10.1029/2021JA029330

Zhang, X.-J., Li, W., Thorne, R. M., Angelopoulos, V., Bortnik, J., Kletzing, C. A., & Hospodarsky, G. B. (2016). Statistical distribution of EMIC wave spectra: Observations from Van Allen Probes. *Geophysical Research Letters*, *43*(24), 12. https://doi.org/10.1002/2016GL071158

Zhang, X. J., Mourenas, D., Artemyev, A. V., Angelopoulos, V., Bortnik, J., Thorne, R. M., et al. (2019). Nonlinear electron interaction with intense chorus waves: Statistics of occurrence rates. *Geophysical Research Letters*, *46*(13), 7182–7190. https://doi.org/10.1029/2019GL083833

Zhang, X. J., Mourenas, D., Artemyev, A. V., Angelopoulos, V., Kurth, W. S., Kletzing, C. A., & Hospodarsky, G. B. (2020). Rapid frequency variations within intense chorus wave packets. *Geophysical Research Letters*, *47*(15), e88853. https://doi.org/10.1029/2020GL088853

Zhang, X.-J., Mourenas, D., Artemyev, A. V., Angelopoulos, V., & Thorne, R. M. (2017). Contemporaneous EMIC and whistler mode waves: Observations and consequences for MeV electron loss. *Geophysical Research Letters*, *44*(16), 8113–8121. https://doi.org/10.1002/2017GL073886

Zhang, X. J., Mourenas, D., Shen, X. C., Qin, M., Artemyev, A. V., Ma, Q., et al. (2021c). Dependence of relativistic electron precipitation in the ionosphere on EMIC wave minimum resonant energy at the conjugate equator. *Journal of Geophysical Research (Space Physics)*, *126*(5), e29193. https://doi.org/10.1029/2021JA029193

Zhang, X. J., Thorne, R., Artemyev, A., Mourenas, D., Angelopoulos, V., Bortnik, J., et al. (2018). Properties of intense field-aligned lower-band chorus waves: Implications for nonlinear wave-particle interactions. *Journal of Geophysical Research (Space Physics)*, *123*(7), 5379–5393. https://doi.org/10.1029/2018JA025390